Light Water Reactor Sustainability Program

Grizzly Model of Multi-Species Reactive Diffusion, Moisture/Heat Transfer, and Alkali-Silica Reaction in Concrete

September 2015

DOE Office of Nuclear Energy

Light Water Reactor Sustainability Program

Grizzly Model of Multi-Species Reactive Diffusion, Moisture/Heat Transfer, and Alkali-Silica Reaction in Concrete

Hai Huang[1], Benjamin Spencer[2] and Guowei Cai[3]

[1]Energy and Environment Science & Technology, INL
[2]Fuel Modeling and Simulation, INL
[3]Dept. of Civil and Environmental Engineering, Vanderbilt University

September 2015

Idaho National Laboratory
Idaho Falls, Idaho 83415

http://www.inl.gov/lwrs

EXECUTIVE SUMMARY

Concrete is widely used in the construction of nuclear facilities for a number of reasons, including its structural strength and ability to shield radiation. The use of concrete in nuclear power plants for containment and shielding of radiation and radioactive materials has made its performance crucial for the safe operation of those facilities. As such, when long term operation is considered for nuclear power plants, it is critical to have accurate and reliable predictive tools to address concerns related to various aging processes of concrete structures and the capacity of structures subjected to aging-related degradation.

The goal of this report is to document progress on the development and implementation of a fully coupled thermo-hydro-mechanical-chemical model in the Grizzly code with the ultimate goal of reliably predicting the long-term performance of concrete structures in nuclear power plants subjected to various aging and degradation mechanisms, such as external chemical attacks and internal volume-changing chemical reactions within concrete structures induced by alkali-silica reactions and long-term exposure to irradiation.

Based on a number of survey reports of concrete aging mechanisms relevant to nuclear power plants and recommendations from researchers in this field, three modules for modeling concrete have been implemented in the Grizzly code in Fiscal Year 2015: (1) a multi-species reactive diffusion model for cement materials; (2) coupled moisture and heat transfer models for concrete; and (3) an anisotropic, stress-dependent, alkali-silica reaction (ASR) induced swelling model.

The multi-species reactive diffusion model was implemented with the objective of modeling aging of concrete structures subjected to a variety of aggressive external chemical attacks (e.g., chloride attack, sulfate attack etc.). It considers multiple processes relevant to external chemical attacks such as diffusion of reactive ions in aqueous phase within pores, equilibrium chemical speciation reactions and kinetic mineral dissolution/precipitation.

The moisture/heat transfer module was implemented to simulate long-term spatial and temporal evolution of the moisture and temperature fields within concrete structures at both room and elevated temperatures. An ability to predict the evolution of temperature and moisture throughout the structure is essential to predicting degradation mechanisms such as ASR and radiation induced swelling, as those mechanisms are dependent on the temperature and moisture.

The ASR swelling model implemented in Grizzly simulates anisotropic expansion of ASR gel under either uniaxial, biaxial and triaxial stress states, and can be run simultaneously with the moisture/heat transfer model and coupled with a variety of elastic and inelastic solid mechanics models.

This report provides detailed descriptions of the governing equations, constitutive models and numerical algorithms of these three modules implemented in Grizzly. In addition, it provides example simulation results and preliminary model validation against experimental data reported in the literature. The close match between the experiments and simulations clearly demonstrates the potential of Grizzly for reliable evaluation and prediction of long-term performance and response of aged concrete structures in nuclear power plants.

Grizzly is built on the MOOSE framework, which provides an inherently multiphysics environment for solving arbitrary coupled systems of partial differential equations. This framework is ideally suited for solving coupled physics equations of the type involved in concrete degradation. Although much progress has been made on modeling some aspects of the concrete degradation problem, significant work remains to develop a complete modeling capability, and will be continued in coming years. Near-term plans include development of nonlinear mechanical models for concrete and reinforcement and models for radiation-induced volumetric expansion.

CONTENTS

FIGURES

TABLES

ACRONYMS

ASR   Alkali-Silica Reaction

NPP   Nuclear Power Plant

THMC   Thermo-Hydro-Mechanical-Chemical

PDE   Partial Differential Equation

ODE   Ordinary Differential Equation

NAE   Nonlinear Algebraic Equation

FEM   Finite Element Method

JFNK   Jacobian-Free Newton-Krylov

XFEM   Extended Finite Element Method

1 Introduction

Concrete is used in the construction of nuclear facilities because it has a number of desirable properties, including its structural strength and ability to shield radiation. Concrete structures can last for hundreds of years, but they have also been known to deteriorate in very short periods of time under adverse conditions. The use of concrete in nuclear facilities for containment and shielding of radiation and radioactive materials has made its performance crucial for the safe operation of the facility.

Long-term degradation of concrete structures in nuclear power plants (NPPs) is influenced by interacting physical (e.g. freeze/thaw, elevated temperature, radiation), chemical (e.g. slow hydration, leaching, volume expansion reactions) and mechanical (e.g. cracking, crushing) processes leading to the changes of the microstructure of cement constituents and the propagation of micro-cracks [1, 2, 3, 4]. Mechanical damage accelerates the chemical degradation by improving the transport properties of water and reactants (e.g. porosity, permeability, reactive surface area). The durability of concrete structures can then be limited as a result of adverse performance of its cement-paste matrix or aggregate constituents (including reinforce wires, rebars and strands) under either physical or chemical attack. In practice, these different processes may occur concurrently to reinforce each other, leading to a tightly coupled thermo-hydro-mechanical-chemical (THMC) multiphysics problem that is computationally challenging for engineering scale concrete structures. In nearly all chemical and physical processes influencing the degradation of concrete structures, dominant factors include transport mechanisms within the pores and cracks and the presence of water.

Based on previous survey reports [1, 2, 3, 4, 5] on concrete degradation in nuclear power plants and recommendations from other researchers, alkali-silica reaction (ASR) and irradiation-induced damage have been identified as concrete aging mechanisms needing high-priority research. Alkali-silica reactions (ASR) are chemical reactions involving alkali ions and hydroxyl ions within cement pore water and certain siliceous constituents that may be present in aggregate materials and can form a gel. As the alkali-silica gel comes in contact with water, swelling occurs, causing pressure that can lead to volumetric expansion, which can then result in cracking, and could eventually lead to complete destruction of the concrete structures [6, 7]. Concrete deterioration due to ASR typically occurs within 10 years after plant construction, but some structures show no sign of deterioration until 15 to 25 years after construction [1, 3]. ASR occurs at a higher rate at elevated temperature. Accurate modeling of ASR related degradation of concrete structures requires a fully coupled moisture/heat transfer and ASR swelling model.

There are two sources for irradiation-related damage of concrete: (1) the bombardment the material by fast and thermal neutrons from the reactor core; and (2) the gamma rays from the reactor core and those produced when neutrons are captured by steel in the vicinity of concrete. The fast neutrons can cause atomic displacements within the concrete matrix, resulting in significant growth of certain aggregate materials such as flint. Gamma rays result in radiolysis of the water in cement paste, which can affect the creep and shrinkage behavior of concrete [8, 9, 1, 4]. The approximate levels of irradiation necessary to cause measurable damage in concrete were reported to be 1×10^{19} neutrons per square centimeter (n/cm^2) for neutron fluence, and 10^{10} rads of gamma radiation dose [10].

Both ASR and radiation-induced volumetric expansion are highly dependent on the temperature and moisture content of concrete. Given the high priority of research on these degradation mechanisms for nuclear concrete structures, significant effort was devoted to implement a fully coupled moisture and heat transfer model in Grizzly, as these models will be used for modeling both degradation mechanisms. This implementation includes a comprehensive set of constitutive models describing transport properties of concrete for moisture and heat. An anisotropic, stress-dependent ASR swelling constitutive model was also implemented. The moisture/heat transfer model, ASR-induced swelling constitutive model and elastic/inelastic solid mechanics models already available in Grizzly collectively form a fully coupled THMC model to address ASR-induced aging issues of concrete structures in nuclear power plants. All variables such as temperature, relative humidity, and displacements are solved in a tightly coupled Newton iteration procedure.

A smaller effort was also devoted to implement a multi-species reactive diffusion model into Grizzly to provide capability for evaluating various external chemical attack scenarios, such as sulfate attack, chloride attack, and carbonation [11, 12, 13, 14, 15, 16, 17, 18, 19, 16, 20, 21], to certain concrete structures in nuclear power power plants (e.g., concrete foundations in contact with soil and groundwater). One important output of this reactive diffusion model is the predictions of the spatial/temporal distributions of pH in concrete pore water, which is critical for evaluating the impact of corrosion of reinforcing steel and associated degradation of concrete structures.

This report provides detailed descriptions of the governing equations, constitutive models and numerical algorithms of these three models implemented in Grizzly, simulation results of demonstration problems and comparison results with experimental data reported in literature. The close match between the experiments and simulations clearly demonstrate the potential of Grizzly for reliable evaluations and predictions of the long-term performance and response of aged concrete structures in nuclear power plants. This report also provides recommendations for future implementations of other aging mechanisms and additional model capability developments and model validations.

2 Coupled reactive diffusion of multiple species in concrete

2.1 Reactive diffusion and external chemical attacks

Because concrete is significantly weaker in tension than compression, reinforcing steel is typically provided for tensile and shear strength, but can also be provided to help resist compressive loads. A minimal amount of reinforcement is required for all structures to resist tensile stresses due to shrinkage and thermal effects [22]. Potential causes of degradation of the mild reinforcing steel are corrosion, elevated temperature, irradiation, and fatigue. Of these, corrosion is the factor of most concern for aging management of concrete structures in nuclear power plants [1].

In dense concrete with low permeability and porosity, the high alkalinity condition within the concrete (typically with pH > 12) causes a passive iron oxide film to form on the iron surface. However, when the pH of pore water falls below 11, a porous oxide layer (rust) forms on the reinforcing steel due to corrosion. Carbonation and the presence of chloride ions can destroy the passive iron oxide film. For example, carbonation reduces the pH of pore water within concrete, leading to corrosion of reinforcing steel and cracking of cement materials nearby, which in turn accelerates the carbonation reactions. The passive iron oxide film on the steel reinforcement can also be destroyed in the presence of chloride ions in pore water, even at high alkalinities (with pH > 11.5), which promotes corrosion [11, 12, 13, 14, 15, 16]. Thus there is a great need to accurately model and simulate the coupled diffusion-reaction processes and predict the spatial-temporal evolution of reactive chemicals dissolved in cement pore water and pH change To reliably evaluate and predict the long-term performance and response of certain concrete structures subjected to aggressive external chemical environment, including foundations in contact with soil and groundwater.

Reactive transport models for chemical-transport simulations of concrete material degradation have various levels of complexity [23, 24, 25, 26, 27, 28]. The simplest type of reactive transport model is that of calcium leaching, which only involves one reactant: calcium in pore water [24]. These models do not consider complex solution-mineral reactions and aqueous speciations and often assume some type of phenomenological reaction and kinetics. More robust reactive transport models should involve multiple reactive species in the aqueous phase, such as those for carbonation and chloride/sulfate attacks [29]. Multi-species reactive transport models that involve full aqueous speciations and pore water-mineral reactions were also developed for predicting spatial and temporal distributions of reactive species in concrete cement [27, 28, 30]. These multi-species reactive transport models allow more accurate predictions of the spatial-temporal evolution of cement mineralogy and solution chemistry. This is especially crucial in the case of complex aggressive solutions containing multiple dissolved ions and reactions with pH buffering (e.g. carbonation reaction). Some reactive transport models ignore fluid flow and associated convective transport of reactive species in the aqueous phase, and only consider molecular diffusion of reactive species [30]. Such an assumption is only valid in the case where there is no significant fluid pressure gradient within and across concrete structures, or the permeability of concrete is too small to allow fluid flow. Permeability and porosity of aging concrete often increase over time due to calcium leaching or microcracking induced by expansive chemical reactions. Under such circumstances, both convective transport and hydrodynamic dispersion [31, 32] need to be considered in reactive transport models.

2.2 Governing equations of reactive diffusion

In Grizzly, the transport of reactive cations and anions from the external environment (e.g. soil and groundwater) is described by the conventional diffusion theory of Fick's law and mass conservation, similar to the chloride diffusion model developed by Xi and Bazant [33]. In addition, processes like aqueous speciation reactions and solution-mineral interactions (in the form of first-order kinetic dissolution and precipitation) were implemented in Grizzly's coupled multi-species reactive diffusion model. A hypothetical sulfate attack

on a concrete foundations is used here as an example to illustrate the multi-species reactive diffusion model. Figure 1 shows the conceptual model used in this example.
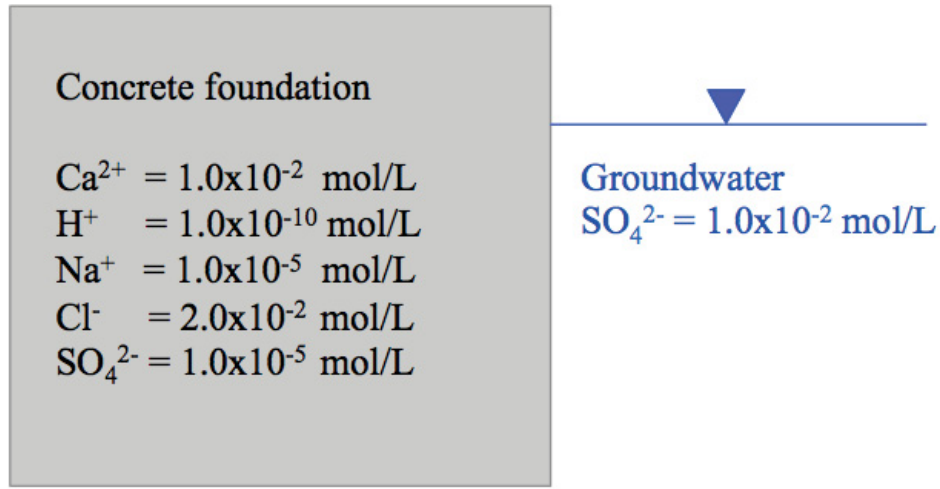
Figure 1: Conceptual model for a hypothetical sulfate attack on a concrete foundation and initial concentrations of primary ions in pore water

Fluid flow and the associated convective transport of reactive ions in and out of concrete are ignored, and only the diffusive transport process of ions is considered. In this hypothetical sulfate attack scenario, groundwater in contact with concrete has a high concentration of sulfate, which will penetrate (via molecular diffusion) into concrete and reacts with calcium ions within the concrete pore water, which usually has a high calcium concentration. This reaction will result in precipitation of gypsum, which in turn changes the porosity and effective diffusivity of cement, leading to a tightly coupled diffusion-reaction system. Further, it is assumed that concrete has an initial porosity of 0.10 and pores are fully saturated with liquid water. Also note that the initial ion concentrations are chosen arbitrarily for demonstration purpose and perhaps do not represent realistic water chemistry. The problem can be described by the following set of coupled partial differential equations (PDEs), ordinary differential equations (ODEs) and nonlinear algebraic equations (NAEs):

$$\frac{\partial[\theta(C_{Ca^{2+}} + C_{CaCl^+} + C_{CaCl_2(aq)} + C_{CaOH^+} + C_{CaSO_4(aq)} + C_{CaSO_4(s)})]}{\partial t} - \nabla[\theta D \cdot \nabla(C_{Ca^{2+}} + C_{CaCl^+} + C_{CaCl_2(aq)} + C_{CaOH^+} + C_{CaSO_4(aq)})] = 0 \tag{1}$$

$$\frac{\partial[\theta(C_{cl}^- + C_{CaCl_2(aq)} + C_{HCl(aq)})] + C_{NaCl(aq)}}{\partial t} - \nabla[\theta D \cdot \nabla(C_{Cl^-} + C_{CaCl^+} + 2C_{CaCl_2(aq)} + C_{NaCl(aq)})] = 0 \tag{2}$$

$$\frac{\partial[\theta(C_{H^+} + 2C_{H_2SO_4(aq)} + C_{HCl(aq)} + C + HSO_4^- - C_{CaOH^+} - C_{NaOH(aq)} - C_{OH^-})]}{\partial t} - \nabla[\theta D \cdot \nabla(C_{H^+} + 2C_{H_2SO_4(aq)} + C_{HCl(aq)} + C_{HSO_4^-} - C_{CaOH^+} - C_{NaOH(aq)} - C_{OH^-})] = 0 \tag{3}$$

$$\frac{\partial\theta(C_{Na^+} + C_{NaCl(aq)} + C_{NaOH(aq)} + C_{NaSO_4^-})}{\partial t} - \nabla[\theta D \cdot \nabla(C_{Na^+} + C_{NaCl(aq)} + C_{NaOH(aq)} + C_{NaSO_4^-})] = 0 \tag{4}$$

$$\frac{\theta(C_{SO_4}^{2-} + C_{CaSO_4(aq)} + C_{H_2SO_4(aq)} + C_{HSO_4^-} + C_{NaSO_4^-} + C_{CaSO_4(s)})}{\partial t} - \nabla[\theta D \cdot \nabla(C_{SO_4^-} + C_{CaSO_4(aq)} + C_{H_2SO_4(aq)} + C_{HSO_4^-} + C_{NaSO_4^-})] = 0 \tag{5}$$

$$\frac{d(C_{CaSO_4(s)})}{dt} - 0.1 \times 6.456542 \times 10^{-8} \times \left(1 - \frac{C_{Ca^{2+}} \cdot C_{SO_4^-}}{10^{-1.8487}}\right) = 0 \tag{6}$$

$$C_{CaCl^+} - 10^{-7}C_{Ca^{2+}} \cdot C_{Cl^-} = 0 \tag{7}$$

$$C_{CaCl(aq)} - 10^{-0.653}C_{Ca^{2+}} \cdot (C_{Cl^-})^2 = 0 \tag{8}$$

$$C_{CaOH^+} - 10^{-12.85}C_{Ca^{2+}} \cdot (C_{H^+}^{-1}) = 0 \tag{9}$$

$$C_{CaSO_4(aq)} - 10^{2.1}C_{Ca^{2+}} \cdot C_{SO_4^-} = 0 \tag{10}$$

$$C_{H_2SO_4(aq)} - 10^{-1.021}(C_{H^+})^2 \cdot C_{SO_4^-} = 0 \tag{11}$$

$$C_{HCl(aq)} - 10^{0.7}C_{H^+} \cdot C_{cl^-} = 0 \tag{12}$$

$$C_{HSO_4^-} - 10^{1.976}C_{H^+} \cdot C_{SO_4^-} = 0 \tag{13}$$

$$C_{NaCl(aq)} - 10^{-0.782}C_{Na^+} \cdot C_{Cl^-} = 0 \tag{14}$$

$$C + NaOH(aq) - 10^{-14.799}C_{Na^+} \cdot (C_{H^+})^{-1} = 0 \tag{15}$$

$$C_{NaSO_4^-} - 10^{0.82}C_{Na^+} \cdot C_{SO_4^-} = 0 \tag{16}$$

$$C_{OH^-} - 10^{-13.991}(C_{H^+})^{-1} = 0 \tag{17}$$

In these equations, D is the effective diffusion coefficient (m^2/s), the θ is the porosity of the cement and the subscripted C variables are the ion concentrations (in mol/L of solution). The reaction constants and parameters in Equations 6-17 are obtained from the EQ3/6 thermodynamics database[34]. One immediately recognizes that these governing equations are highly nonlinear and tightly coupled, thus need to be solved in a fully coupled manner.

2.3 Simulation results
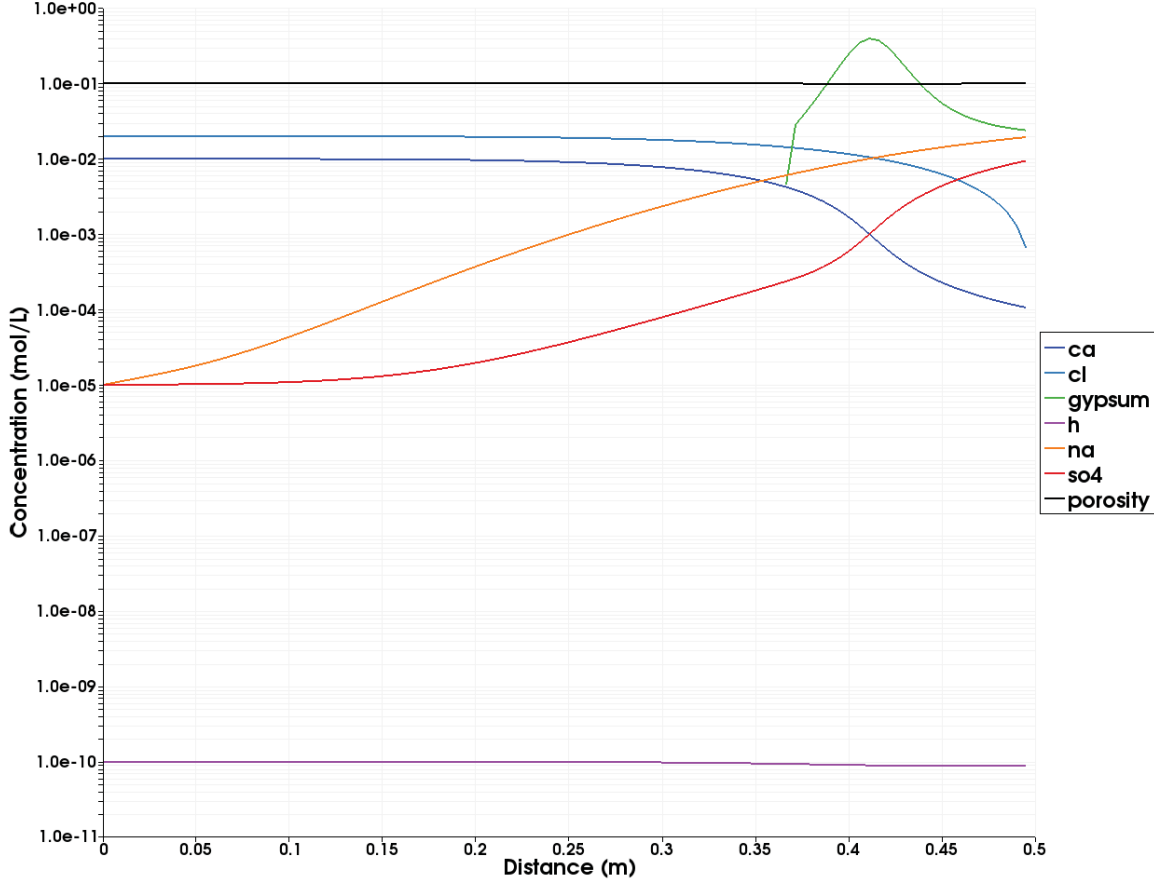
Figure 2: Concentration profiles of major reactive aqueous species, precipitated mineral and associated porosity change after 5 years of sulfate intrusion into the concrete

Because it provides natural support for solving tightly coupled systems of PDEs, Grizzly is an ideal platform for solving these equations. Figure 2 shows the simulated concentration profiles of major reactive aqueous ions and associated precipitated mineral amount and porosity changes at a time of 5 years after sulfate intrusion started. It clearly shows that as sulfate in groundwater diffuses into concrete, it reacts with calcium in cement pore water, resulting in precipitation of mineral gypsum and reduction of the concentrations of both calcium and sulfate within the reaction zone. It is also interesting to observe a slight reduction in free proton H^+ concentration (indicating slight increase in pH) within the reaction zone, which is consistent with the aqueous solution chemistry defined by Equations 6-17. Other external chemical attacks such as chloride attack and carbonation might induce much larger pH variations in concrete pore water. Only a small reduction of porosity can be observed in the simulation results due to the use of a small mineral dissolution/precipitation

rate constant used in the simulation. Despite the strong nonlinearity of the governing equations, both linear and nonlinear iterations converge very well.

2.4 Reaction network definition

One of the challenging task in modeling coupled multi-species reactive diffusion problems in concrete structures is to define the reaction network (also referred as reaction pathways) and provide all required reaction rate parameters and equilibrium constants, such as those shown in Equations 6-17 for the hypothetical sulfate attack example problem. A module known as `ReactionNetwork` has been implemented in Grizzly to facilitate the convenient definition of the reaction network by code users in the input file, following a generic chemical reaction syntax. Figure 3 shows an example usage of `ReactionNetwork` in the input file for this hypothetical sulfate attack problem, which greatly simplifies the input file syntax and provides a convenient way to setup simulations for multi-species reactive diffusion problems. Users can conveniently define the primary aqueous species and their initial concentrations in concrete pore water, and secondary aqueous species that are the products of aqueous speciation reactions among primary species. All reaction rate parameters and equilibrium constants of aqueous speciation reactions are obtained from EQ3/6 thermodynamics database [34]. Although in this example problem only one mineral was defined in the input file, the `ReactionNetwork` module in Grizzly allows users to conveniently specify multiple reactive minerals and their initial compositions in concrete texture. Those minerals can react with the pore water in concrete and follow various dissolution/precipitation kinetics, with rate parameters specified by users.

```
[ReactionNetwork]
 primary_aqueous_species    = 'ca       cl      h       na      so4'
 initial_condition          = '1.0e-2 1.0e-5 1.0e-10 1.0e-5 1.0e-5'

# aqueous speciations
 secondary_aqueous_species = 'cacl cacl2_aq caoh caso4_aq h2so4_aq hcl_aq hso4 nacl_aq naoh_aq naso4 oh'
 aqueous_speciations       = '(1.0)ca + (1.0)cl  = (1.0)cacl       -0.7
                              (1.0)ca + (2.0)cl  = (1.0)cacl2_aq  -0.653
                              (1.0)ca + (-1.0)h  = (1.0)caoh      -12.85
                              (1.0)ca + (1.0)so4 = (1.0)caso4_aq    2.1
                              (2.0)h  + (1.0)so4 = (1.0)h2so4_aq  -1.021
                              (1.0)h  + (1.0)cl  = (1.0)hcl_aq      0.7
                              (1.0)h  + (1.0)so4 = (1.0)hso4       1.976
                              (1.0)na + (1.0)cl  = (1.0)nacl_aq   -0.782
                              (1.0)na + (-1.0)h  = (1.0)naoh_aq  -14.799
                              (1.0)na + (1.0)so4 = (1.0)naso4       0.82
                              (-1.0)h            = (1.0)oh       -13.991'
# mineral-solution reactions
 minerals = 'gypsum'
 initial_mineral_conc = '0.0'
 mineral_solution_reactions = '(1.0)ca+(1.0)so4=gypsum'
 log_k = '-6'
 specific_reactive_surface_area = '0.1'
# kinetic_rate_constant = '6.456542e-3'
 kinetic_rate_constant = '6.456542e-4'
 activation_energy = '1.5e4'
 gas_constant = 8.314
 reference_temperature = 298.15
 system_temperature = 298.15
□
```

Figure 3: Example usage of the `ReactionNetwork` module in the Grizzly input file for the hypothetical sulfate attack problem

3 Coupled moisture and heat transfer model

Concrete degradation generally stems from more than one cause. These various aging mechanisms, including freeze-thaw cycles, expansive chemical reactions, irradiation-induced damage mineral dissolution and precipitation, and corrosion of reinforcing steel, often act closely together and all involve water. Furthermore, it is well known that ASR reactions are often thermally activated [35, 36, 37]. Therefore, accurate predictions of aging behavior of concrete structures first requires accurate predictions of the spatial and temporal evolution of the moisture and temperature fields within concrete structures. Most of the existing numerical models developed to deal with degradation phenomena of concrete structures are based on fluid flow and transport theory of porous media [31, 32], and only consider the effect of one or a small subset of the aging mechanisms [38, 39, 21, 40, 41, 42, 43, 44, 45, 46, 47, 48, 49, 50, 51, 52, 53, 54, 55, 56, 57, 58]. The majority of these developed models are typically limited to a simplified moisture diffusion model for fluid flow, in which various phases, such as vapor, dry air and liquid water filling the pores, are modeled as an equivalent fluid [59, 60, 61, 62].

Saouma et al. [63] recently compiled a comprehensive set of constitutive models and parameters for moisture diffusion and heat transfer in concrete. The equivalent moisture diffusion/heat transfer model [59, 60, 61, 62] has been implemented in Grizzly, along with the full set of constitutive models compiled by Saouma et al.[63]. This section provides detailed descriptions of the governing equations and associated constitutive laws for the coupled moisture diffusion and heat transfer model.

3.1 Heat transfer model

3.1.1 Governing equation

The governing partial differential equation for heat transfer in concrete is given by Bazant et al. [60] and Saouma et al. [63] as:

$$\rho C \frac{\partial T}{\partial t} = \frac{\partial}{\partial x}\left(k\frac{\partial T}{\partial x}\right) + \frac{\partial}{\partial y}\left(k\frac{\partial T}{\partial y}\right) + \frac{\partial}{\partial z}\left(k\frac{\partial T}{\partial z}\right) - C_w \mathbf{J}\nabla T + C_a \frac{\partial W}{\partial H}\frac{\partial H}{\partial t} + Q, \qquad (18)$$

where:

ρ	=	density in kg/m^3
C	=	specific heat of concrete in J/kg°C
T	=	temperature in °C
k	=	thermal conductivity of concrete in W/m°C
C_w	=	mass density and isobaric (constant pressure) heat capacity of liquid water
$\mathbf{J}$	=	moisture flux, $-D_h\nabla\mathbf{H}$
W	=	water (moisture) content in g/g (for unit volume of material, m^3)
H	=	pore relative humidity
C_a	=	heat absorption of free water in J/kg
$\frac{\partial W}{\partial H}$	=	moisture capacity in g/gm^3
Q	=	rate of heat per unit volume generated within the body W/m^3
t	=	time in s

The first term on the right side of Equation 18 represents the thermal conduction; the second term represents the convective transport of heat due to fluid flow; and the third term represents adsorption heat due to adsorption of free water molecules in pores onto pore walls. The mass density and isobaric (constant

8

pressure) heat capacity of liquid water C_w is given by

$$C_w = \rho_{water} C_{water},\tag{19}$$

where ρ_{water} is mass density of liquid water in kg/m^3 which is given as [64]

$$\rho_{water} = 314.4 + 685.6 \left[1 - \left(\frac{T - 273.15}{374.14} \right)^{\frac{1}{0.55}} \right]^{0.55},\tag{20}$$

and C_{water} is the isobaric (constant pressure) heat capacity of liquid water in J/kg°C. The values of C_{water} are tabulated in [65]. The adsorption heat C_a usually can be neglected according to Bazant et al. [60]. Thus, in Grizzly, a small fraction of the concrete specific heat capacity C value is simply assigned to C_a (i.e., $C_a = 0.001 \times C$).

3.1.2   Thermal capacity

Following Saouma et al. [63], four constitutive models were implemented in Grizzly for concrete thermal capacity ρC (in MJ/m^3°C): (1) a user-supplied constant thermal capacity; (2) the American Society Civil Engineering (ASCE) model [66] for normal-strength concrete; (3) the Kodur model [67] for high-strength concrete and (4) the Eurocode model [68] for both normal- and high-strength concrete. Details of these models are provided below:

- **Constant**
  In this model, the user provides a value of ρC that remains constant during the simulation.

- **ASCE [66]**
  Siliceous aggregate concrete

$$\rho C = \begin{cases} 0.005T + 1.7 & \text{for} \quad 20°C \le T \le 200°C \\ 2.7 & \text{for} \quad 200°C \le T \le 400°C \\ 0.013T - 2.5 & \text{for} \quad 400°C \le T \le 500°C \\ 10.5 - 0.013T & \text{for} \quad 500°C \le T \le 600°C \\ 2.7 & \text{for} \quad T > 600°C \end{cases}\tag{21}$$

Carbonate aggregate concrete

$$\rho C = \begin{cases} 2.566 & \text{for} \quad 20°C \le T \le 400°C \\ 0.1756T - 68.034 & \text{for} \quad 400°C \le T \le 410°C \\ 25.00671 - 0.05043T & \text{for} \quad 410°C \le T \le 445°C \\ 2.556 & \text{for} \quad 445°C \le T \le 500°C \\ 0.01603T - 5.44881 & \text{for} \quad 500°C \le T \le 635°C \\ 0.16635T - 100.90225 & \text{for} \quad 635°C \le T \le 715°C \\ 176.07343 - 0.22103T & \text{for} \quad 715°C \le T \le 785°C \\ 2.566 & \text{for} \quad T > 785°C \end{cases}\tag{22}$$

Note that ρC is in units of MJ/m^3°C in this particular thermal capacity model.

- **Kodur [67]**
  Siliceous aggregate concrete

$$\rho C = \begin{cases} 0.005T + 1.7 & \text{for} \quad 20°C \leq T \leq 200°C \\ 2.7 & \text{for} \quad 200°C \leq T \leq 400°C \\ 0.013T - 2.5 & \text{for} \quad 400°C \leq T \leq 500°C \\ 10.5 - 0.013T & \text{for} \quad 500°C \leq T \leq 600°C \\ 2.7 & \text{for} \quad 600°C \leq T \leq 635°C \end{cases} \tag{23}$$

Carbonate aggregate concrete

$$\rho C = \begin{cases} 2.45 & \text{for} \quad 20°C \leq T \leq 400°C \\ 0.026T - 12.85 & \text{for} \quad 400°C \leq T \leq 475°C \\ 0.0143T - 6.295 & \text{for} \quad 475°C \leq T \leq 650°C \\ 0.1894T - 120.11 & \text{for} \quad 650°C \leq T \leq 735°C \\ -0.263T + 212.4 & \text{for} \quad 735°C \leq T \leq 800°C \\ 2.0 & \text{for} \quad 800°C \leq T \leq 1000°C \end{cases} \tag{24}$$

Note that ρC is in units of MJ/m^3°C in this particular thermal capacity model.

- **Eurocode [68]**
  The equation for density of concrete (in kg/m^3) is given by

$$\rho = \begin{cases} \rho_{ref} & \text{for} \quad 20°C \leq T \leq 115°C \\ \rho_{ref}\left(1 - \frac{0.02(T-115)}{85}\right) & \text{for} \quad 115°C \leq T \leq 200°C \\ \rho_{ref}\left(0.98 - \frac{0.03(T-200)}{200}\right) & \text{for} \quad 200°C \leq T \leq 400°C \\ \rho_{ref}\left(0.95 - \frac{0.07(T-400)}{800}\right) & \text{for} \quad 400°C \leq T \leq 1200°C \end{cases} \tag{25}$$

where ρ_{ref} is reference concrete density at 20°C and the equation for specific heat of concrete (in J/kg°C) is given by

$$C = \begin{cases} 900 & \text{for} \quad 20°C \leq T \leq 100°C \\ 900 + (T - 100) & \text{for} \quad 100°C \leq T \leq 200°C \\ 1000 + \left(\frac{T-200}{2}\right) & \text{for} \quad 200°C \leq T \leq 400°C \\ 1100 & \text{for} \quad 400°C \leq T \leq 1200°C \end{cases} \tag{26}$$

3.1.3 Thermal conductivity

Also Following Saouma et al. [63], four thermal conductivity models were implemented in Grizzly, all depending on the temperature and concrete texture, including (1) a user-supplied constant thermal conductivity (2) the ASCE model [66] for normal-strength concrete at high temperature; (3) the Kodur model [67] for high-strength concrete; (4) the Eurocode model [68] for both normal- and high-strength concrete; and (5) the Kim model [69]. Details of these models are provided below:

- **Constant**
  In this model, the user provides a value of k that remains constant during the simulation.

- **ASCE [66]**

  Siliceous aggregate concrete

  $$k = \begin{cases} -0.000625T + 1.5 & \text{for} \quad 20°\text{C} \leq T \leq 800°\text{C} \\ 1.0 & \text{for} \quad T > 800°\text{C} \end{cases} \tag{27}$$

  Carbonate aggregate concrete

  $$k = \begin{cases} 1.355 & \text{for} \quad 20°\text{C} \leq T \leq 293°\text{C} \\ 1.0 & \text{for} \quad T > 293°\text{C} \end{cases} \tag{28}$$

- **Kodur [67]**

  Siliceous aggregate concrete

  $$k = 0.85(2 - 0.0011T) \quad \text{for} \quad 20°\text{C} \leq T \leq 1000°\text{C} \tag{29}$$

  Carbonate aggregate concrete

  $$k = \begin{cases} 0.85(2 - 0.0013T) & \text{for} \quad 20°\text{C} \leq T \leq 300°\text{C} \\ 0.85(2.21 - 0.002T) & \text{for} \quad T > 300°\text{C} \end{cases} \tag{30}$$

- **Eurocode [68]**

  Upper limit

  $$k = 2 - 0.2451 \left(\frac{T}{100}\right) + 0.0107 \left(\frac{T}{100}\right)^2 \quad \text{for} \quad 20°\text{C} \leq T \leq 1200°\text{C} \tag{31}$$

  Lower limit

  $$k = 1.36 - 0.136 \left(\frac{T}{100}\right) + 0.0057 \left(\frac{T}{100}\right)^2 \quad \text{for} \quad 20°\text{C} \leq T \leq 1200°\text{C} \tag{32}$$

- **Kim [69]**

  $$k = \lambda_H \lambda_{S/A} \lambda_T \lambda_{AG} k_{ref} \tag{33}$$

  $$\lambda_H = 0.9[1.62 - 1.54(w/c)] + 0.2H \tag{34}$$

  $$\lambda_{S/A} = 0.86 + 0.36(S/A) \tag{35}$$

  $$\lambda_T = 1.05 - 0.0025T \tag{36}$$

  $$\lambda_{AG} = 0.293 + 1.01AG \tag{37}$$

  in which

  $$\begin{aligned} H &= \text{relative humidity} \\ AG &= \text{aggregate volume} \\ S/A &= \text{fine aggregate fraction} \\ w/c &= \text{water to cement ratio} \\ T &= \text{temperature} \end{aligned}$$

These various heat transfer constitutive models can be conveniently chosen and specified from input file. It is also noteworthy to mention that the heat transfer model in Grizzly can be run alone, without considering moisture diffusion.

3.2   Moisture diffusion

Many physical and chemical aging mechanisms of concrete strongly depend on the presence and mobility of water within concrete pores. Thus moisture diffusion has a very important role in the long-term performance of concrete structures. It is now widely recognized that modeling of concrete as a variably saturated porous medium and multiphase system is a more rigorous approach for the mass and heat transport processes that occur in concrete exposed to environments [50]. Thus, more general three-field flow models for flow of vapor, air and liquid water in variably saturated porous media have been developed by a number of authors based on multiphase flow and transport theory of unsaturated, deformable, porous media [70, 71, 72, 39]. However, implementation of such general nonisothermal, multiphase flow and heat transport model requires a significant effort, and has not yet been done in Grizzly. This is an area for future work.

In Grizzly, a simpler, quite popular moisture diffusion model in concrete based on the work of Xi, Bazant and Molina [62] was implemented. This moisture diffusion model simply lumps different phases of fluids in concrete pores into an equivalent fluid characterized by pore relative humidity H, which is related to pore vapor pressure P_v via $H = P_v/P_{vs}$, where P_{vs} is the saturated vapor pressure at a given temperature T. Saouma et al. [63] compiled and provided a comprehensive set of constitutive models and parameters for moisture diffusion in concrete structures, which were also implemented in the Grizzly code. Detailed descriptions of the governing equation and constitutive models for moisture diffusion are provided here.

3.2.1   Governing equation

Following Saouma et al. [63], the governing equation for moisture diffusion in concrete is formulated by using relative humidity H as the primary variable:

$$\frac{\partial W}{\partial H}\frac{\partial H}{\partial t} = \nabla(D_h \nabla H) + \nabla(D_{ht}\nabla T) + \frac{\partial W_d}{\partial t}, \tag{38}$$

where

W = total water content (g/g) (for unit volume of concrete, cm^3)

H = pore relative humidity, and $H = P_v/P_{vs}$

P_{vs} = saturate vapor pressure $= P_{atm}e^{\left(4871.3\frac{T-100}{373.15T}\right)}$
(Bary and Poryet (2012) (T is the temperature in K))

P_{atm} = standard atmospheric pressure $= 101.325 Pa$

D_h = moisture diffusivity (also referred as humidity diffusivity) (cm^2/day)

D_{ht} = coupled moisture diffusivity under the influence of a temperature gradient in cm^2/day

W_d = total mass of free evaporable water released into the pores
by dehydration of the cement paste

t = time (day)

Two important parameters, moisture capacity $\partial W/\partial H$ and moisture diffusivity D_h, both depend on the relative humidity H. Thus the moisture diffusion governing equation is highly nonlinear. The following sections describes in detail the constitutive models for this two parameters. Also it is worth noting that since the relative humidity strongly depends on the temperature T, the moisture diffusion model in Grizzly is always coupled with heat transfer model described in the previous section.

3.2.2   Moisture capacity

Xi et al. [61, 62] developed a concrete moisture capacity model based on the Brunauer-Emmett-Teller (BET) adsorption isotherm theory, which was implemented in Grizzly. The total water content W in concrete at a

constant temperature T is referred as water adsorption isotherm, which was proposed by Xi et al. [61] as:

$$W = \frac{CkV_mH}{(1 - kH)[1 + (C - 1)kH]},$$

(39)

where

$$
\begin{aligned}
C &= \exp\left(\frac{C_0}{T}\right), C_0 = 855 \\
H &= \text{relative humidity} \\
T &= \text{absolute temperature in } K \\
W &= \text{quantity of vapor absorbed at pressure } p \\
&\quad (\text{g water/g cement}) \\
V_m &= \text{monolayer capacity: mass of adsorbate required to cover} \\
&\quad \text{the adsorbent with a single molecular layer} \\
k &= \text{empirical constant}
\end{aligned}
$$

The monolayer capacity, V_m, is defined as the mass of adsorbate required to cover the surface of the adsorbent with a single molecular layer. To evaluate W at a given relative humidity value, V_m and the empirical constant k in the above equation need to be evaluated first. This is done separately for cement and aggregate materials as follows:

- **Monolayer capacity, V_m**

    - **Cement Paste:**

$$V_m = V_t(t)V_{wc}(w/c)V_{ct}(ct)V_T(T),$$

(40)

where t is the age of concrete material in $days$; $V_{ct}(ct)$ represents the effect of cement types on the adsorption isotherm and is given by Table 1; $V_T(T) = 1$ at room temperature and remains constant during simulations, and

$$V_t(t) = \begin{cases} 0.068 - \frac{0.22}{t} & for \quad t > 5 \quad days \\ V_t(5) & if \quad t \leq 5 \quad days \end{cases}$$

(41)

$$V_{wc}(w/c) = \begin{cases} 0.85 + 0.45\frac{w}{c} & for \quad 0.3 < w/c < 0.7 \\ V_{wc}(0.3) & if \quad w/c \leq 0.3 \end{cases}$$

(42)

$V_t(t)$ represents the effects of concrete age and $V_{wc}(w/c)$ represents the effect of water to cement ratio w/c on the adsorption isotherm, respectively.

Table 1: V_{ct} for different types of concrete

	Concrete Type			
	1	2	3	4
V_{ct}	0.9	1.0	0.85	0.6

Table 2: V_{ag} of various pore structure of aggregate

Pore structure of aggregate	V_{ag}
dense	$0.05 - 0.1$
porous	$0.1 - 0.04$

– **Aggregates:**
The monolayer capacity V_m of aggregates is determined by

$$V_m = 0.00647V_{ag},\qquad(43)$$

where V_{ag} depends on the pore structure of various aggregates as listed in Table 2.

• **Empirical constant k**
The empirical constant k in Equation 39 is related to the the number of layers of adsorbed water molecule, n, under saturated state. n is determined separately for cement and aggregate materials.

– **Cement Paste:**
n is expressed in terms similar to those of V_m:

$$n = N_t(t)N_{wc}(w/c)N_{ct}(ct)N_T(T)\qquad(44)$$

$$N_t(t) = \begin{cases} 2.5 + \frac{1.5}{t_e} & for \quad t > 5 \quad days \\ 5.5 & if \quad t \leq 5 \quad days \end{cases}\qquad(45)$$

$$N_{wc}(w/c) = \begin{cases} 0.33 + 2.2\frac{w}{c} & for \quad 0.3 < w/c < 0.7 \quad days \\ N_{wc}(0.3) & if \quad w/c \leq 0.3 \\ N_{wc}(0.7) & if \quad w/c \geq 0.7 \end{cases}\qquad(46)$$

where $N_{ct}(ct)$ is given by Table 3 and $N_T(T) = 1$ at room temperature and remains constant during the simulation.

Table 3: N_{ct} for different types of concrete

	Concrete Type			
	1	2	3	4
N_{ct}	1.1	1.0	1.15	1.5

– **Aggregates:**
For the aggregate, n is expressed as:

$$n = 4.603n_{ag}\qquad(47)$$

where n_{ag} is defined in Table 4.

Once the number of adsorbed layers of molecule, n, is obtained, k can be obtained by

$$k = \frac{\left(1 - \frac{1}{n}\right)C - 1}{C - 1}.\qquad(48)$$

Table 4: n_{ag} of various pore structure of aggregate

Pore structure of aggregate	n_{ag}
dense	$1.0 - 1.5$
porous	$1.7 - 2.0$

Finally, once the monolayer capacity V_m and empirical constant k are obtained, then using Equation 39, the water content W in cement and aggregate materials can be obtained. The moisture capacities for cement paste or aggregate material can also be determined by taking derivatives of both sides of Equation 39 with respect to relative humidity H as

$$\frac{\partial W}{\partial H}\Big|_{cp;agg} = \frac{CkV_m + WK[1 + (C-1)kH] - Wk(1-kH)(C-1)}{(1-kH)[1+(C-1)kH]}.$$ (49)

The total moisture capacity of the concrete structure $\frac{\partial W}{\partial H}$ required by the moisture diffusion governing equation (38) is then simply the weight-average value between cement and aggregate materials as:

$$\frac{\partial W}{\partial H} = f_{agg}\left(\frac{\partial W}{\partial H}\right)_{agg} + f_{cp}\left(\frac{\partial W}{\partial H}\right)_{cp},$$ (50)

where

$\begin{aligned}
f_{agg} &= \text{weight percentage of the aggregate} \\
f_{cp} &= \text{weight percentage of the cement paste} \\
\left(\frac{\partial W}{\partial H}\right)_{agg} &= \text{moisture capacity of aggregate (g/g)} \\
&\quad \text{(for the unit volume of material, cm}^3\text{)} \\
\left(\frac{\partial W}{\partial H}\right)_{cp} &= \text{moisture capacity of cement paste (g/g)} \\
&\quad \text{(for the unit volume of material, cm}^3\text{)}
\end{aligned}$

The total moisture capacity $\partial W / \partial H$ (with the units of g water/g material) is a function of water content W, temperature T and relative humidity H, and strongly depends on the concrete texture.

3.2.3   Moisture diffusivity

The moisture diffusivity of concrete D_h is a complex function of temperature T, relative humidity H and pore structure of concrete. Various diffusion mechanisms often interact, such as molecular diffusion in large pores (usually 50nm - 10 microns and beyond) and microcracks, Knudson diffusion in mesopores (2.5nm - 50 nm) and micropores (<2.5nm) and surface diffusion along pore walls [63]. Most existing moisture diffusivity models typically do not account for individual diffusion mechanisms separately. Instead, they tend to reproduce the general combined trend.

In Grizzly, calculation of D_h starts with the calculation of a reference moisture diffusivity $D_{h,0}$ at a given temperature T and relative humidity H. Three reference moisture diffusivity $D_{h,0}$ models are implemented as:

- **Xi (in units of cm^2/day) [73]**

$$D_{h,0} = D_{Hcp} \left[1 + \frac{g_i}{\frac{1-g_i}{3} + \frac{1}{\frac{D_{Hagg}}{D_{Hcp}} - 1}} \right], \tag{51}$$

where

$$
\begin{array}{lcl}
D_{h,0} & = & \text{humidity diffusion coefficient of concrete (cm}^2\text{/day)} \\
D_{Hcp} & = & \text{humidity diffusion coefficient of cement paste (cm}^2\text{/day)} \\
D_{Hagg} & = & \text{humidity diffusion coefficient of aggregate (cm}^2\text{/day)} \\
g_i & = & \text{the volume fraction of aggregate}
\end{array}
$$

The humidity diffusion coefficient, D_{Hcp}, for cement paste is expressed as:

$$D_{Hcp} = \alpha_h + \beta_h \left[1 - 2^{-10\gamma_h(H-1)} \right] \tag{52}$$

$$\alpha_h = 1.05 - 3.8\frac{w}{c} + 3.56 \left(\frac{w}{c} \right)^2 \tag{53}$$

$$\beta_h = -14.4 + 50.4\frac{w}{c} - 41.8 \left(\frac{w}{c} \right)^2 \tag{54}$$

$$\gamma_h = 31.3 - 136\frac{w}{c} + 162 \left(\frac{w}{c} \right)^2 \tag{55}$$

where α_h, β_h and γ_h are coefficients from test data. Since the value of the humidity diffusivity coefficient for aggregates, D_{Hagg}, typically is negligible compared with the value of D_{Hcp}, it is assumed to be zero in the current implementation.

- **Mensi (in units of m^2/s) [74]**

$$D_{h,0} = Ae^{BC}, \tag{56}$$

where $A = 3.8 \times 10^{-13}$ and $B = 0.05$ are constants. C is the free water content in L/m^3, and is a function of relative humidity H in concrete as given by

$$C = HC_0, \tag{57}$$

where C_0 is constant takes a value of 130 (in L/m^3).

- **Bazant (in units of m^2/s) [60]**

$$D_{h,0} = D_1 f_H, \tag{58}$$

where $D_1 = 3.10 \times 10^{-10} m^2/s$ and

$$f_H = \begin{cases} \alpha_D + \dfrac{1-\alpha_D}{1+\left(\frac{1-H}{1-0.75} \right)^n} & for \quad T \leq 95°C \\ 1 & for \quad T > 95°C \end{cases} \tag{59}$$

Also, $f_H = 1$ when $H > 1$ and α_D is given by

$$\alpha_D = \frac{1}{1 + \frac{19(95-T)}{70}} \tag{60}$$

where T is in °C. $\alpha \in [0.037 : 1]$ from $T \in [0°C : 95°C]$ and $n \in [6 : 16]$.

It's obvious that all three reference moisture diffusivity models strongly depend on the value of humidity H, and indirectly on the temperature T. Once the value of reference moisture diffusivity $D_{h,0}$ is obtained, the actual concrete moisture diffusivity D_h required by the moisture diffusion governing equation, (38), can then be calculated by

$$D_h = \begin{cases} D_{h,0} f_1(T) & for \quad T \leq 95°C \\ D_{h,0} f_1(95°C) f_2(T) & for \quad T > 95°C \end{cases} \tag{61}$$

where

$$f_1(T) = e^{\frac{Q}{R}\left(\frac{1}{T_{ref}} - \frac{1}{T}\right)} \quad for \quad T \leq 95°C, \tag{62}$$

in which T is the absolute temperature (K), Q is activation energy for water migration along the adsorption layers in the necks, and R is gas constant with Q/R=2700 K, and

$$f_2(T) = e^{\frac{T-95}{0.881+0.214(T-95)}} \quad for \quad T > 95°C. \tag{63}$$

3.2.4   Dehydrated water W_d

The amount of dehydrated water W_d (in units g water/g material per 1 cm³ volume of material) behaves like a source term in the moisture diffusion governing equation, and represents the water molecules released into concrete pores due to dehydration of hydrated minerals within cement paste as the temperature in concrete increases. W_d is given by the following empirical formula:

$$W_d = W_H^{105} f_d(T), \tag{64}$$

in which W_H^{105} is the hydrated water content (in units of g water/g material per 1 cm³ volume of material) at 105 °C, and f_d is a function of the weight loss of the concrete due to heat. Dehydration of hydrated minerals within cement paste typically begins at about 120 °C.

The function of W_H is given by

$$W_H(t_e) = 0.21c(\frac{t_e}{\tau_e + t_e}), \quad \tau_e = 23 \quad \text{days} \tag{65}$$

where c is mass of (anhydrous) cement per cm³ of concrete and t_e is the equivalent hydration period which is given by

$$t_e = \int \beta_H \beta_T dt \tag{66}$$

$$\beta_H(H) = \frac{1}{1 + (3.5 - 3.5H)^4} \tag{67}$$

$$\beta_T(T) = e^{\frac{Q_h}{R}(\frac{1}{T_{ref}} - \frac{1}{T})} \tag{68}$$

where

17

$$
\begin{array}{rcl}
t & = & \text{actual time} \\
Q_h & = & \text{activation energy of hydration} \\
\dfrac{Q_h}{R} & = & 2700 \text{ K}
\end{array}
$$

Typical values of $f_d(T)$ are plotted by Harmathy and Allen [75]. In Grizzly, a simple linear function

$$
f_d(T) = \frac{0.05T}{600}, \tag{69}
$$

is implemented to account for mass loss of concrete due to dehydration. It is interesting to note that W_d is often negligible in modeling moisture diffusion under most circumstances unless the concrete is subjected to rapid heating conditions at high temperature. It is also interesting to note that by extending the definition of W_d to hydrated water, the same model can also be applied to simulate the moisture distribution in concrete during curing process. In such case, W_d becomes a sink term and represents the loss of free water molecules in pores due to hydration reactions.

3.2.5   Coupled moisture diffusion by thermal gradient D_{ht}

It has been reported by Bazant et al. [60] that the additional moisture diffusion due to thermal gradients included in the moisture governing equation is negligible. Thus the value of D_{ht} is set to 0.0 by default in Grizzly. Users can, however, set this parameter to an arbitrary value if desired.

3.3   Summary of numerical solution method

In Grizzly, the governing moisture diffusion equation (38), and the heat transfer equation (18), are discretized by finite element method (FEM) and implicitly solved simultaneously to provide a fully coupled solution for the relative humidity H and temperature T, using a Jacobian-Free Newton-Krylov (JFNK) solution procedure [76]. The JFNK solution approach to nonlinear problems has a similar nonlinear convergence rate of the traditional Newton's method, but without explicitly computing and storing the full Jacobian matrix. Therefore, it has the advantage for solving large multiphysics problems, and is the default solution method in Grizzly for modeling coupled THMC processes in concrete structures.

During each Newton-Krylov iteration, the thermal and moisture transport properties such as ρC, k, $\partial W / \partial H$, D_h, W_d and D_{ht} are evaluated first on every quadrature point within each element, given the values of the temperature T and relative humidity H from the last iteration. These new material properties are then used to calculate new residual values for the current iteration, so that the converged solution incorporates all coupling effects between the physics.

Independent material property modules are used to compute the thermal and moisture properties at the quadrature points. These models are passed in values of variables on which they depend, such as H and T. These variables can either be primary solution variables, as is the case for a fully coupled scenario, or arbitrary prescribed variables, which would permit a single-physics computation. This modular and flexible code architecture greatly facilitates the development of models and introducing new couplings between other physics, which is critical for modeling the coupled multiphysics phenomena involved in concrete aging processes.

3.4   Coupled moisture/thermal model validation

An initial validation of the coupled moisture diffusion and heat transfer model in Grizzly is shown here. A detailed comparison was made between simulation results and data from a large-scale reinforced concrete

heating experiment (MAQBETH mock-up) performed by the French Atomic Energy Commission (CEA Saclay)[77]. Saouma et al. [63] recently used the same MAQBETH experimental data to validate their coupled moisture/heat transfer model, which is the same model implemented in Grizzly.

The MAQBETH mock-up is a reinforced hollow concrete cylinder with inner and outer diameters of 1.0 and 2.2m, respectively, and a height of 3m, as shown in Figures 4 and 5. This structure was heated to 200 °C from the inside of the hollow cylinder and maintained at 200 ° C for several hundred hours. The outside surface of the concrete cylinder was cooled by convective heat transfer to the air, as shown in Figure 5, which produced a significant thermal gradient in the radial direction. Several sensors were placed at a number of radial positions inside the structure to measure the spatial and temporal evolution of temperature, gas pressure and relative humidity.
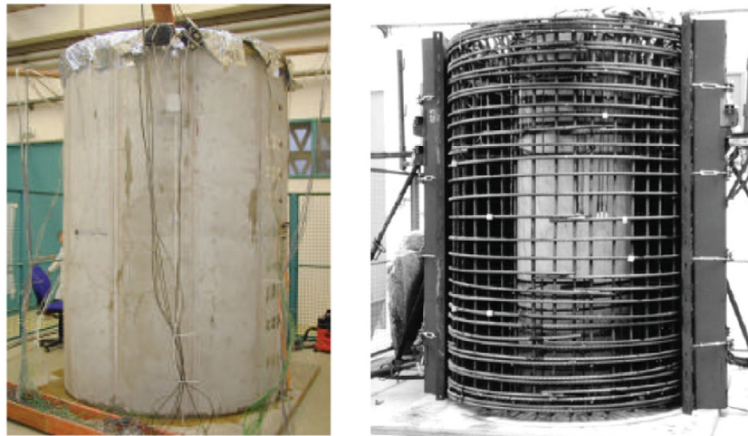

Figure 4: General view of MAQBETH mock-up (left) and cylindrical steel reinforcement (from [77])
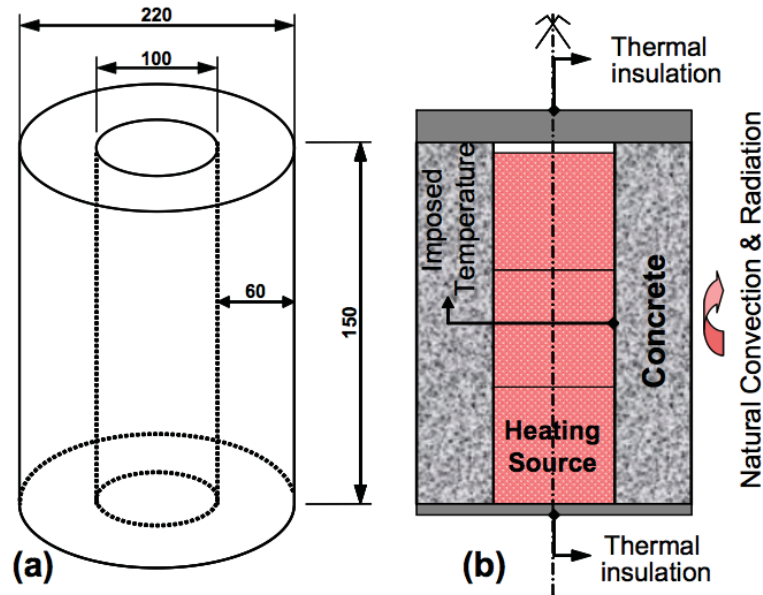

Figure 5: Geometric characteristics of MAQBETH mock-up concrete hollow cylinder (a) (from [77]) and schematic description of the experiment (b) (from [78])

Due to the axisymmetric nature of both the concrete cylinder and the thermal boundary conditions, it is appropriate to model it using a 2D axisymmetric representation. In addition, a symmetry plane normal to the axial direction can be employed. This approach was used in a Grizzly model of this experiment. Figure 6 shows the initial and boundary conditions of the 2D axial symmetric model used in our simulation. Similar to [78], the initial temperature T and relative humidity H are 20 °C and 0.96, respectively. A constant vapor pressure of 2,500 Pa is applied to both the inner and outer surfaces for moisture diffusion. A convective heat transfer boundary is applied to the outer surface with a constant air temperature of 20 °C and heat exchange coefficient $h=10$ W/m^2°C. The loading temperature as shown in Figure 6 is directly applied to the inner surface as prescribed temperature boundary condition. The top and bottom surfaces are modeled as insulated boundaries for heat transfer and no-flux boundaries for moisture transfer.
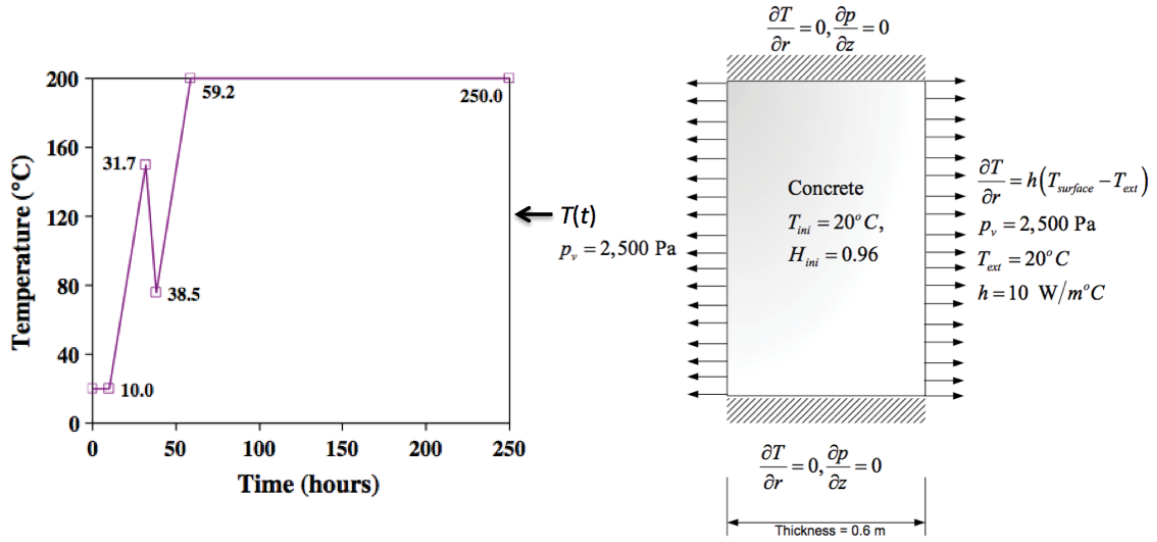
Figure 6: Initial conditions and time history of boundary conditions applied to the 2D axial symmetric model (modified from [63] and [78]). The thermal loading history on the inner surface is shown on the left.

The concrete composition and characteristics of the MAQBETH mock-up are listed in Table 5. This information was used to select appropriate constitutive models and associated parameters used in the simulation. Specifically, the Kodur models were chosen for both thermal capacity and thermal conductivity, and the Bazant moisture diffusivity model was chosen for moisture diffusion. In this simulation, the effect of steel reinforcing bars on the thermal and moisture diffusion processes was ignored due to their small total volumetric fraction in the structure. The reinforcing steel bars would have a dramatic impact on the mechanical behavior of the structure, so they would need to be included in a simulation that included mechanical deformation.

Figure 7 shows the 2D axial symmetric finite element mesh used in the simulations, and contours of the simulated temperature and relative humidity fields at the time 250 hours after the heating started. To resolve the steep gradients of the relative humidity near both the inner and outer surfaces, the mesh was refined in the radial direction near both surfaces. It is obvious that the heating near the inner surface dries up the adjacent concrete and leads to the reduction of pore relative humidity (i.e. the reduction of moisture content). It is also worth mentioning that because of the low moisture diffusivity of the concrete, the simulated relative humidity field exhibits steep gradients near both the inner and outer surfaces of the hollow concrete cylinder.

Quantitative comparisons of the temperature and relative humidity profiles obtained from the experiment and simulation were performed at various times. Figure 8 presents the numerical and experimental (symbols)

Table 5: Concrete composition in MAQBETH experiment [78].

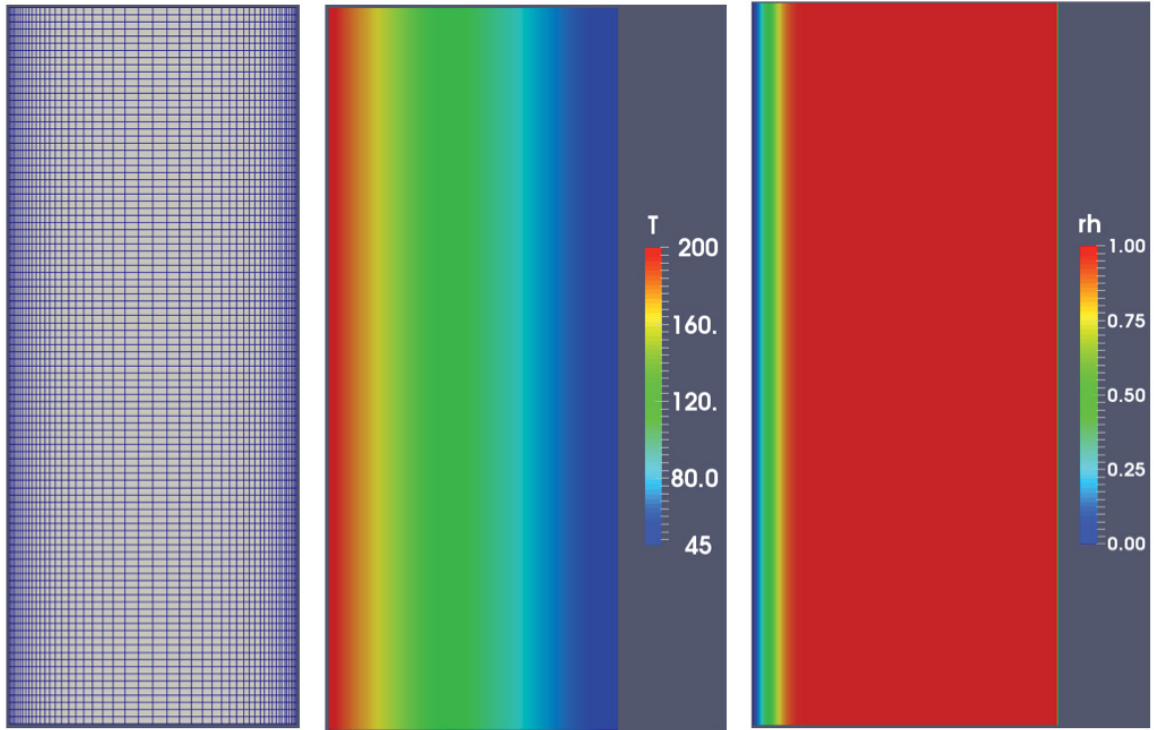| Data	Value
Cement mass m_c (CEM I 52,5 Lafarge)	354 kg/m^3
Aggregate mass m_a	1877 kg/m^3
Calcium-siliceous gravel 5-20 mm	715 kg/m^3
Fine calcium-siliceous gravel 5-14 mm	402 kg/m^3
Siliceous sand $0 - 5mm$	760 kg/m^3
Mix water m_w	154 kg/m^3
Superplasticizer optima 100	5.31 kg/m^3
Water/cement ratio	0.43 kg/m^3
Hydrated water d_0	$0.9 \times 0.21 \times m_c$ kg/m^3

Figure 7: Finite element mesh (left), simulated temperature field (middle) and relative humidity field (right) at the time 250 hours after the heating started.

radial profiles of the temperature at various times. In this plot, radial distances of 0 and 0.6*m* correspond to the inner and outer surfaces of the hollow concrete cylinder, respectively. The simulated temperature profiles are in good agreement with the experimental measurements, although some minor discrepancies appear at various sensor locations, perhaps due to measurement or sensor location perturbations caused by steel rebars [78]. Both the simulation results and experimental measurements indicate that the temperature field approaches steady state at 126 hours after the start of heating. The satisfactory match demonstrate that the model correctly reproduces the temperature evolution inside the concrete structure.
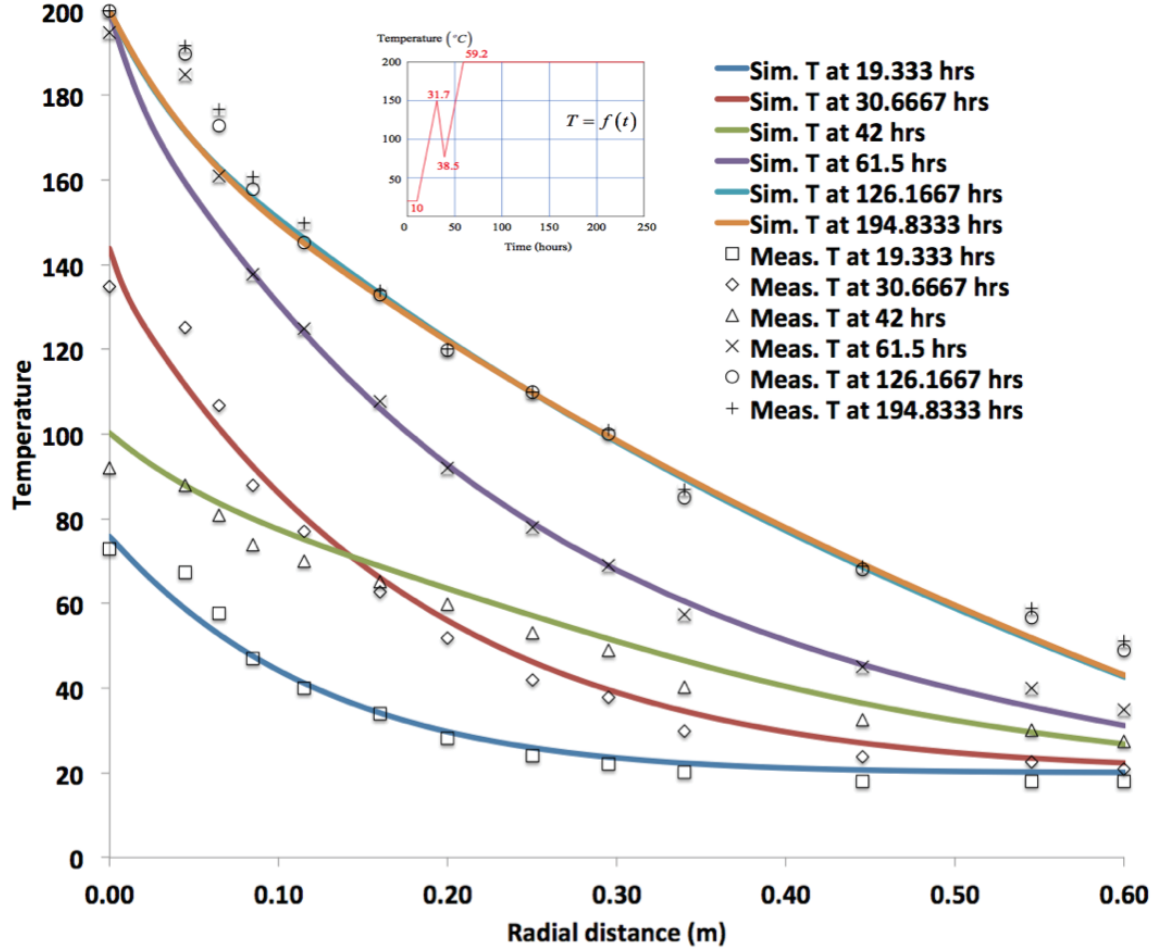
Figure 8: Comparisons of radial temperature profiles at various times between the simulation (lines) and experimental measurements (symbols).

Figure 9 presents the numerical and experimental radial profiles of the relative humidity at various times. The simulated relative humidity profiles are in reasonably good agreement with the experimental results. Upon heating at the inner surface, due to the fixed vapor pressure there, the concrete is dried near the inner surface first, and moisture in the interior of the structure diffuses toward the heated inner surface and escapes, leading to a drying front that gradually propagates into the interior of the structure. Also notable is that near the heated inner surface, the relative humidity is approaching 0, and near the outer surface, the relative humidity exhibits a sharp gradient over a short distance of about 1-2 cm. Grizzly exhibits very good convergence when solving this numerically challenging simulation.

Figure 10 shows the spatial distributions of the humidity (moisture) diffusivity D_h and moisture capacity
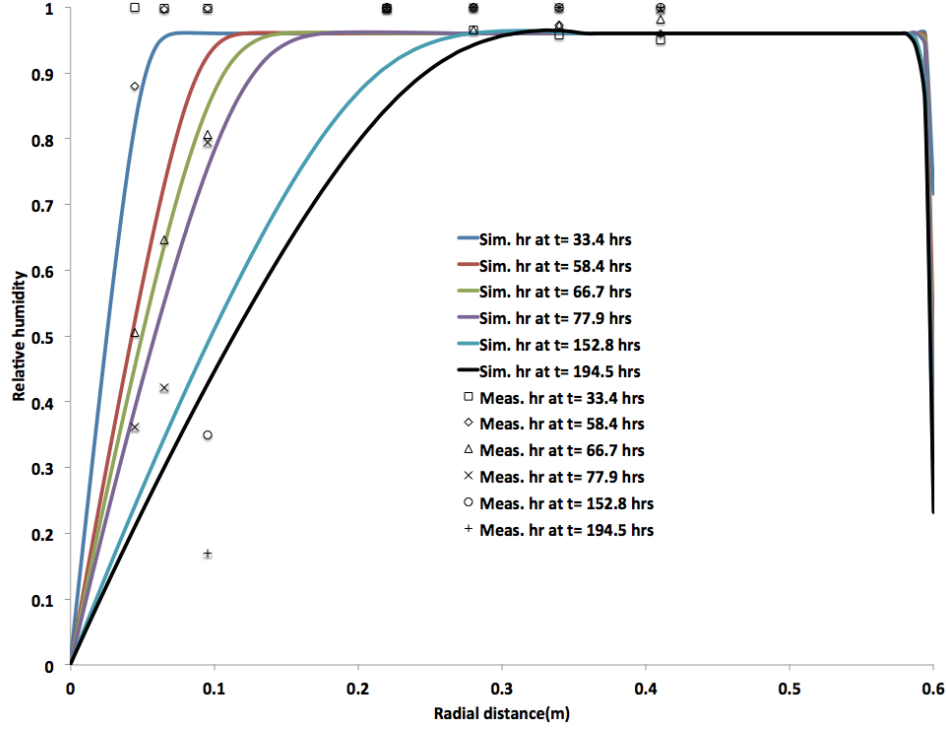
Figure 9: Comparisons of radial relative humidity profiles at various times between the simulation (lines) and experimental measurements (symbols).

$\partial W/\partial H$ within the concrete structure at the time 200 hours after the start of heating. The whole concrete structure starts with constant values of D_h and $\partial W/\partial H$ before heating. Due to the strong dependency of these two moisture transport properties on the temperature T and relative humidity H, strong spatial variations in D_h and $\partial W/\partial H$ appear as they evolve with the transient temperature and relative humidity fields. This demonstrates the necessity of a fully coupled solution strategy for such a coupled thermal/moisture diffusion model.

Grizzly allows for simulations to be performed in 1, 2 or 3 dimensions. This capability was demonstrated by simulating the MAQBETH experiment in 3D. Figure 11 shows the 3D mesh, and the simulated temperature and relative humidity fields at the time 200 hours after heating started. These 3D simulation results are in almost perfect agreement with those obtained from the previous 2D axial symmetric model, as shown in Figure 12.
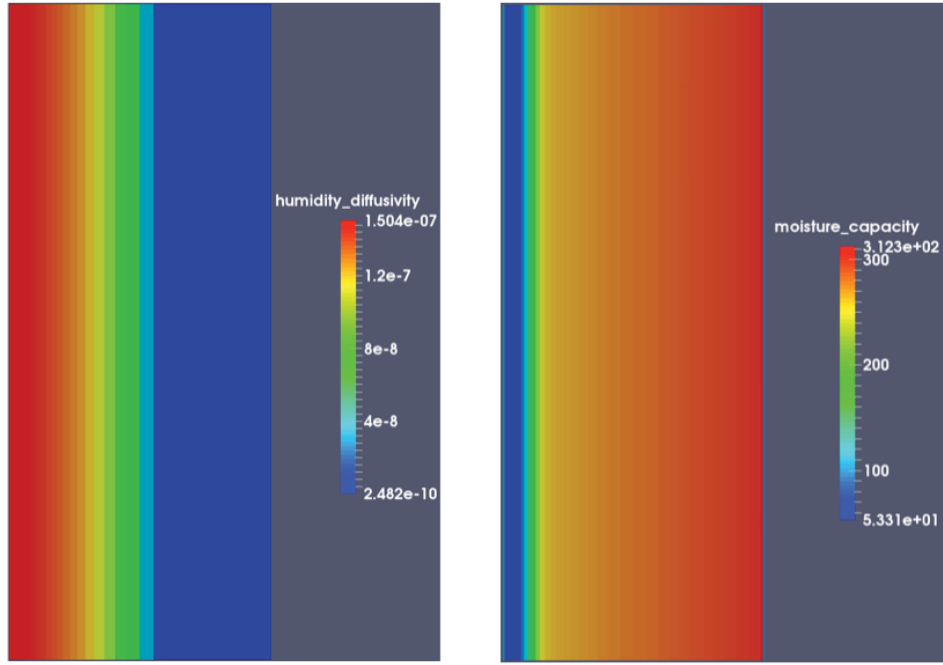
Figure 10: Spatial distributions of the humidity diffusivity D_h (left) and moisture capacity $\partial W / \partial H$ (right) at 200 hours.
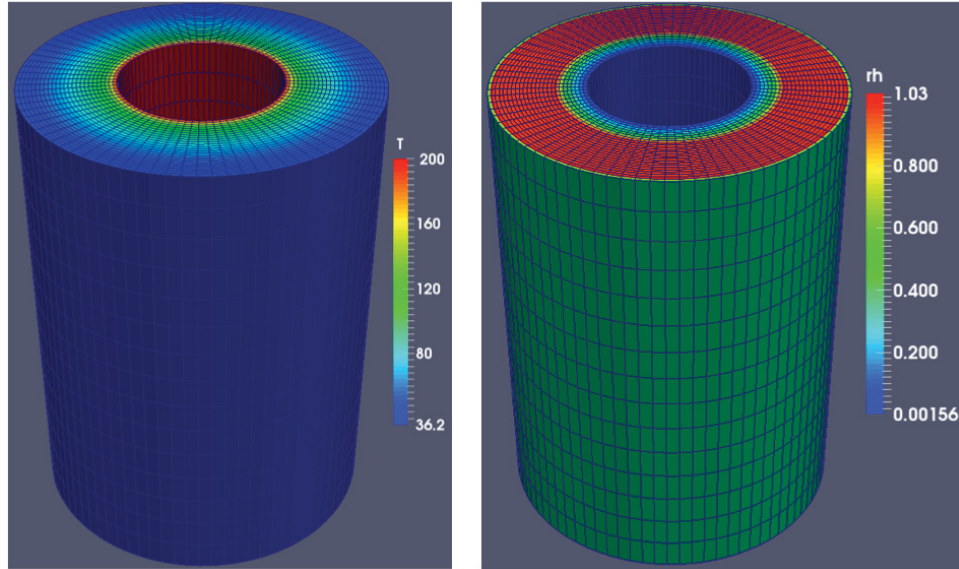
Figure 11: Simulated temperature (left) and relative humidity fields (right) at 200 hours obtained from a full 3D model.
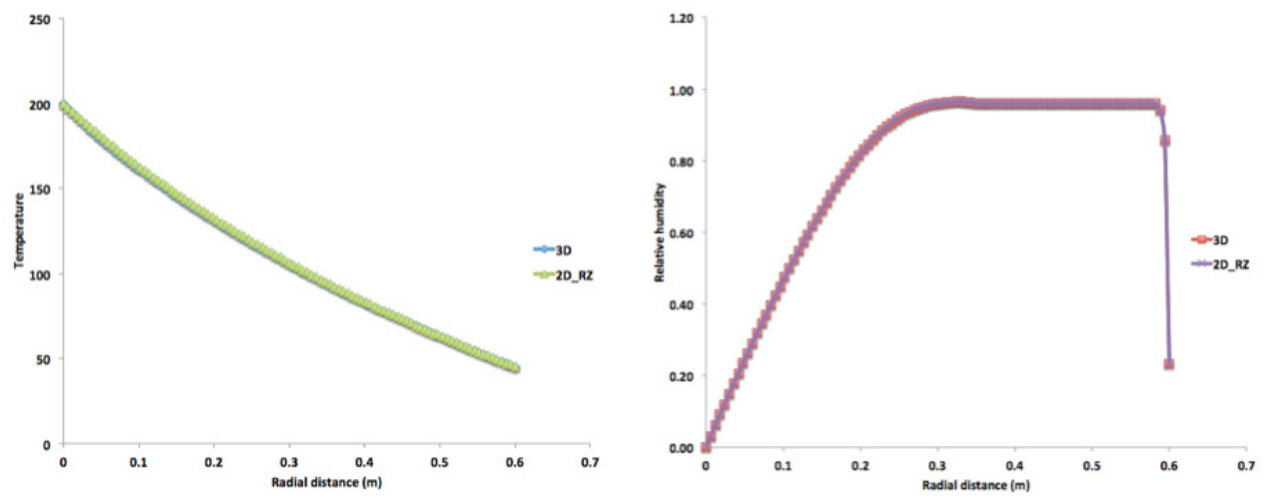
Figure 12: Comparisons of the simulated temperature (left) and relative humidity (right) profiles at 200 hours from the full 3D and 2D axial symmetric models.

4 Alkali-silica reaction (ASR) swelling model

ASR deterioration to concrete structures can be attributed, on the microscopic level, to the formation of a hydrophilic gel due to complex dissolution-precipitation reactions between reactive silica in aggregates, alkaline ions such as potassium K^+ and Na^+ and hydroxyl ions OH^- in the cement pore solution. If water is available in concrete pores, the gel swells, creating an internal pressure in localized regions within concrete structures, which can initiate micro- and macrocracking, excessive expansion, misalignment of the structure etc. According to [37], there are two important factors that control the ASR reaction rate:

- ASR reactions are thermally activated. The higher the temperature, the faster they occur. This kinetic effect of temperature on ASR results from the thermoactivation of both the dissolution of reactive silica on aggregate-cement interface and the precipitation of gel.

- The relative humidity in concrete has a strong influence on ASR, affecting both the kinetics and magnitude of volumetric swelling. Water plays an important role as a solvent for silica dissolution, intervenes as a transport medium for diffusion of ions through the pore network, and is a necessary compound for the formation of various reaction products (gels and other mineral precipitates).

Therefore, accurate predictions of the effects of ASR on long-term performance and response of aged concrete structures requires a fully coupled thermo-hydro-mechanical-chemical (THMC) model. Among many ASR related models developed over the past a few decades, it is worth noting a thermodynamically consistent coupled thermo-chemo-mechanics model of ASR developed by Ulm et al. [37] based on an extensive experimental study by Larive [79], which departs from other empirical models. However, it does not include the effect of the stress state on the reaction kinetics and volumetric swelling, and only considers isotropic swelling. Farage et al. [80] further extended Ulm et al.'s model by including a smeared cracking approach to model cracking of concrete due to ASR expansion. However, only heat conduction was considered, and the moisture diffusion was not considered in these coupled thermo-chemical-mechanics models. One more serious limitation of these ASR swelling models is that the swelling stain is treated isotropically without stress dependence.

Saouma and Perotti [35] presented a comprehensive coupled THMC model for ASR swelling based on the model of Ulm et al, and considered the effects of stress on both the ASR reaction kinetics and anisotropic volumetric expansion. Saouma and Perotti's ASR model is perhaps the most scientifically rigorous and represents the state of the art in modeling ASR expansion, which includes the following features [35]:

- The ASR expansion strain is treated as as a full strain tensor, not calculated independently for each principal direction;

- The ASR reaction rate is temperature dependent;

- The ASR reaction can be retarded by compressive stress within concrete structures;

- The ASR expansion is constrained by compression, and is redirected into other less-constrained principal directions;

- Both high compressive or tensile stress states inhibit ASR expansion due to the formation of micro- and macro-cracks that adsorb the expanding gel;

- Triaxial compressive stress states reduce expansion;

- The tensile strength and elastic modulus are reduced due to ASR reactions.

Saouma and Perotti's ASR swelling model [35] has been implemented in Grizzly. Detailed descriptions of the constitutive models for ASR reaction kinetics and ASR-induced anisotropic expansion are provided here.

4.1 1ˢᵗ-order ASR reaction kinetics

Based on Ulm et al.'s stress-independent reaction [37], Saouma and Perotti proposed a 1ˢᵗ-order ASR reaction kinetics model that is dependent on both the temperature and the first invariant of the stress tensor [35] as:

$$t_C(\theta,\xi) \cdot \frac{d\xi}{dt} = \tau_C(\theta) \cdot \frac{1 + exp[-\tau_L(\theta, I_\sigma, f_c')/\tau_C(\theta)]}{\xi + exp[-\tau_L(\theta, I_\sigma, f_c')/\tau_C(\theta)]} \cdot \frac{d\xi}{dt} = 1 - \xi, \tag{70}$$

in which ξ is the ASR reaction extent ranging from 0 (not reacted) to 1 (fully reacted), θ is the temperature (note that the symbol θ is used instead of T for temperature to be consistent with the notations in [37] and [35], and $\tau_C(\theta)$ and $\tau_L(\theta, I_\sigma, f_c')$ are expressed as

$$\tau_C(\theta) = \tau_C(\theta_0)exp[U_C(1/\theta - 1/\theta_0)] \tag{71}$$
$$\tau_L(\theta, I_\sigma, f_c') = f(I_\sigma, f_c')\tau_L(\theta_0)exp[U_L(1/\theta - 1/\theta_0)] \tag{72}$$

representing the latency and characteristic times of ASR reactions, respectively. Here θ_0 is the reference temperature (i.e., the temperature at which stress-free ASR experiments are carried out), I_σ is the first invariant of the stress tensor, f_c' is the uniaxial compressive strength of concrete, and U_L and U_C are thermal activation energy constants for the latency and characteristic times, respectively, and are determined from Larive's tests [79] as

$$U_L = 9400 \pm 500K \tag{73}$$
$$U_C = 5400 \pm 500K \tag{74}$$

The function $f(I_\sigma, f_c')$ in Equation 72 represents the effect of compressive stress on the ASR reaction kinetics by modifying the latency time τ_L and is defined as [35]

$$f(I_\sigma, f_c') = \begin{cases} 1 & if \quad I_\sigma > 0 \\ 1 + \alpha\frac{I_\sigma}{3f_c'} & if \quad I_\sigma \leq 0 \end{cases}, \text{where } I_\sigma = \sigma_\text{I} + \sigma_\text{II} + \sigma_\text{III}. \tag{75}$$

Saouma and Perotti [35] assumed a value of 4/3 for the constant α based on their analysis of some experimental data. When I_σ is greater than zero (i.e., tensile stress state), $f(I_\sigma, f_c')$ equals 1, indicating no effect of tensile stress on the reaction kinetics. When I_σ is less than zero (i.e., compressive stress state), $f(I_\sigma, f_c')$ has a value greater than 1, indicating an increase in the latency time τ_L (equivalently retardation of ASR reaction).

Equation 70 for the ASR reaction is a nonlinear ordinary differential equation (ODE) that can be solved locally (i.e, on the quadrature points within elements) by a Newton-Raphson iteration scheme, given the current temperature, stress tensor and the reaction extent at the end of the previous time step. To be consistent to the solid mechanics solver in Grizzly, where an incremental strain (stress) formulation approach was adopted, Equation 70 is reformulated in terms of incremental ASR reaction extent $\Delta\xi$ from time t to $t + \Delta t$ and written in residual form as:

$$\begin{aligned} F(\Delta\xi) &= t_C(\theta^{t+\Delta t}, \xi^{t+\Delta t}) \cdot \frac{\xi^{t+\Delta t} - \xi^t}{\Delta t} - 1 + \xi^{t+\Delta t} \\ &= t_C(\theta^{t+\Delta t}, \xi^t + \Delta\xi) \cdot \frac{\Delta\xi}{\Delta t} - 1 + (\xi^t + \Delta\xi) \\ &= 0 \end{aligned} \tag{76}$$

4.2 Stress-dependent ASR volumetric strain $\Delta\varepsilon_{vol}^{ASR}$

Once the increment of ASR reaction extent $\Delta\xi$ is obtained, the ASR volumetric strain increment $\Delta\varepsilon_{vol}^{ASR}$ from time t to $t + \Delta t$ is then evaluated using the following formula

$$\Delta\varepsilon_{vol}^{ASR} = \Gamma_t(f_t', \sigma_I | COD)\Gamma_c(\bar{\sigma}, f_c')g(H)\Delta\xi\varepsilon^{\infty}|_{\theta=\theta_0}, \tag{77}$$

where f_t' is the tensile strength of the concrete; σ_I is the maximum principal stress (> 0 under tensile stress); COD is the crack opening displacement; $\bar{\sigma}$ is the ratio between the hydrostatic stress and compressive strength of concrete, and ε^{∞} is the laboratory-determined maximum free volumetric expansion at the reference temperature θ_0.

The function $g(H)$ in Equation 77 accounts for the dependency of gel expansion on the water in concrete and takes the form [35]:

$$g(H) = H^m, \tag{78}$$

where the exponent m is an empirical constant and H is the relative humidity in concrete. $g(H)$ has a value between 0 and 1. For studies of concrete dams, one can reasonably assume $g(H)$ has a value of 1. For various concrete structures, however, $g(H)$ has to be determined by either lab experiments or parameter fitting.

Function $\Gamma_t(f_t', \sigma_I | COD)$ in Equation 77 accounts for the reduction of ASR expansion due to tensile cracking (e.g., gels are adsorbed into tensile macrocracks), and takes the following form [35]:

$$\Gamma_t = \begin{cases} \text{Elasticity} & \begin{aligned} & 1 & if & (\sigma_I \leq \gamma_t f_t') \\ & \Gamma_r + (1 - \Gamma_r)\frac{\gamma_t f_t'}{\sigma_I} & if & (\gamma_t f_t' \leq \sigma_I) \end{aligned} \\ \\ \text{Smeared crack} & \begin{aligned} & 1 & if & COD_{max} \leq \gamma_t f_t' < \sigma_I \\ & \Gamma_r + (1 - \Gamma_r)\frac{\gamma_t W_c}{COD_{max}} & if & Y_t W_c < COD_{max} \end{aligned} \end{cases} \tag{79}$$

in which γ_t is the fraction of the tensile strength beyond which gel is adsorbed by cracks and is a user input parameter in simulation, and Γ_r is a residual ASR expansion retention factor for ASR under tension. The ASR swelling has currently only been implemented in conjunction with an elasticity model. Although a smeared crack model is already available in Grizzly, the function Γ_t has only been implemented for use with elastic material.

Function $\Gamma_c(\bar{\sigma}, f_c')$ in Equation 77 accounts for the reduction in ASR volumetric expansion under compressive stress state, in which gel is absorbed by diffused microcracks, and takes the following form [35]:

$$\Gamma_c = \begin{cases} 1 & if & \bar{\sigma} \leq 0 & \text{tension} \\ 1 - \frac{e^{\beta\bar{\sigma}}}{1+(e^{\beta}-1)\bar{\sigma}} & if & \bar{\sigma} > 0 & \text{compression} \end{cases} \tag{80}$$

$$\bar{\sigma} = \frac{\sigma_I + \sigma_{II} + \sigma_{III}}{3f_c'} \tag{81}$$

where the exponent β is an empirical constant (between -2 and 2 according to [35] and $\bar{\sigma}$ is the ratio between the hydrostatic stress and compressive strength of concrete.

4.3 Anisotropic ASR strains and weights in principal directions

The incremental ASR volumetric stain $\Delta\varepsilon_{vol}^{ASR}$ needs to be redistributed along three principal directions according to their relative propensity for expansion. Saouma and Perotti [35] presented a method to calculate

the relative weights along three principal directions based on the principal stresses under either uniaxial, biaxial or triaxial confinement conditions. Details of their approach for calculating the redistribution weights of ASR volumetric strain in principal directions are provided here, along with details on and its implementation in Grizzly. The notations of Saouma and Perotti [35] are again followed here.

Given the full stress tensor (in Cartesian coordinates) on a quadrature point within an element, an eigensolver is used to obtain the three principal stresses, σ_k, σ_l and σ_m, and associated eigenvectors for the directions of principal stresses, R_k, R_l and R_m. These eigenvectors form a stress/strain rotational matrix $R = (R_k, R_l, R_m)$ that will be used later to rotate the incremental ASR strain tensor expressed in principal stress/strain coordinates back into Cartesian coordinates.
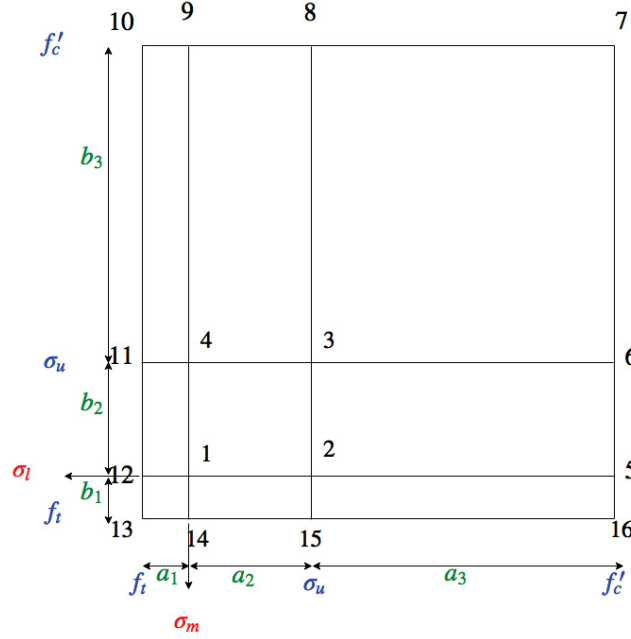
Figure 13: 2D stress-space map and ASR weight interpolation quadrants (modified from [35])

The weight allocation scheme for the principal directions starts by dividing the stress space into nine quadrants using the concrete tensile strength f_t and compressive strength f_c' as well as a gel expansion-inhibiting compressive stress σ_u, as shown in Figure 13. σ_u is defined as the compressive stress beyond which no further gel expansion can occur. Saouma and Perotti [35] proposed a value of $-10MPa$ based on previous experimental studies [79]. Any combination of two principal stresses will fall into one of the nine quadrants of this two-dimensional stress map, which has a total of 16 nodes.

To calculate the ASR expansion weight along the direction of a particular principal stress, using σ_k for example, the following three steps are needed [35]:

- Identify the quadrant encompassing the other two principal stresses σ_l and σ_m using Figure 13 and the corresponding nodal numbers of that quadrant;

- Find the rows of Table 6 corresponding to the identified nodal numbers and determine the nodal weights $W_i(\sigma_k), i = 1, 2, 3, 4$ from the last 3 columns of Table 6 in the corresponding rows using a linear interpolation of σ_k.

Table 6: Triaxial weights (from [35])

Nodal number	σ_l	σ_m	Weight direction k		
			$\sigma_k \leq 0$	$\sigma_k = \sigma_u$	$\sigma_k = f'_c$
1	0	0	1/3	0	0
2	σ_u	0	1/2	0	0
3	σ_u	σ_u	1	1/3	0
4	0	σ_u	1/2	0	0
5	f_c	0	1/2	0	0
6	f_c	σ_u	1	1/2	0
7	f_c	f_c	1	1	1/3
8	σ_u	f_c	1	1/2	0
9	0	f_c	1/2	0	0
10	f_t	f_c	1/2	0	0
11	f_t	σ_u	1/2	0	0
12	f_t	0	1/3	0	0
13	f_t	f_t	1/3	0	0
14	0	f_t	1/3	0	0
15	σ_u	f_t	1/2	0	0
16	f_c	f_t	1/2	0	0

- Finally, compute the ASR expansion weight $W_k(\sigma_k, \sigma_l, \sigma_m)$ for the principal direction k using the four nodal weights of the quadrant in which where (σ_l, σ_m) falls using a bilinear interpolation:

$$W_k(\sigma_k, \sigma_l, \sigma_m) = \Sigma_{i=1}^4 N_i(\sigma_l, \sigma_m) W_i(\sigma_k), \tag{82}$$

where N_i is the bilinear shape function similar to those used in finite element method and is given by

$$N(\sigma_l, \sigma_m) = \frac{1}{ab} \lfloor \ (a - \sigma_l)(b - \sigma_m), \quad \sigma_l(b - \sigma_m), \quad \sigma_l \sigma_m, \quad (a - \sigma_l)\sigma_m \ \rfloor \tag{83}$$

$$W(\sigma_k) = \lfloor \ W_1(\sigma_k), \quad W_2(\sigma_k), \quad W_3(\sigma_k), \quad W_4(\sigma_k) \ \rfloor^T \tag{84}$$

$$a = (a_1|a_2|a_3) \quad b = (b_1|b_2|b_3) \tag{85}$$

$$\sigma_l = (\sigma_l|\sigma_l - \sigma_u) \quad \sigma_m = (\sigma_m|\sigma_m - \sigma_u) \tag{86}$$

The previous steps are then repeated for calculating the ASR expansion weights along the other two principal directions, $W_l(\sigma_k, \sigma_l, \sigma_m)$ and $W_m(\sigma_k, \sigma_l, \sigma_m)$. Note that the summation of W_k, W_l and W_m equals to 1. The individual incremental ASR strains along the principal directions are then obtained using these relative weights by the following formula:

$$\Delta\varepsilon_i^{ASR} = W_i \Delta\varepsilon_V^{ASR}, \quad i = 1, 2 \quad and \quad 3. \tag{87}$$

Unlike isotropic ASR swelling models, the incremental ASR strains along principal directions obtained by the above formula are in general different from each other, depending on the local stress state driven by the material confinement conditions.

Finally, the full ASR expansion-induced incremental strain tensor $\Delta\varepsilon^{ASR}$ on quadrature points can then be conveniently obtained by rotating $\Delta\varepsilon_i^{ASR}$ into the current coordinates via

$$\Delta\varepsilon^{ASR} = R\{\Delta\varepsilon_i^{ASR}\}R^T. \tag{88}$$

in which $\Delta\epsilon^{ASR}$ is a 'chemically' imposed incremental strain tensor at each quadrature point, which is used by the solid mechanics model in Grizzly to drive the deformation of concrete structures.

4.4 Reduction of elastic modulus and tensile strength

The ASR-induced deterioration of concrete mechanical properties is simply modeled as time-dependent function of ASR reaction extent $\xi(t,\theta)$ following Saouma and Perotti [35]:

$$E(t,\theta) = E_0[1 - (1 - \beta_E)\xi(t,\theta)] \tag{89}$$

$$f_t(t,\theta) = f_{t,0}[1 - (1 - \beta_f)\xi(t,\theta)] \tag{90}$$

where E_0 and $f_{t,0}$ are the original elastic modulus and tensile strength, respectively, and β_E and β_f are the corresponding residual fractional values when the concrete has fully reacted, i.e. ϵ_{ASR} tends to ϵ_{ASR}^{∞}. Both β_E and β_f are parameters input by the user.

4.5 Summary of the ASR expansion algorithm

In Grizzly, the calculation of the full ASR-induced incremental strain tensor $\Delta\epsilon^{ASR}$ on each quadrature point in each FEM element is performed by a separate volumetric ASR expansion material model, which takes the values of the temperature, relative humidity and stress from the last Newton-Krylov iteration as input. Note that the stress is also a material property calculated on quadrature points by another separate material model that is used in the solution of the PDEs governing mechanical deformation. To calculate $\Delta\epsilon^{ASR}$, the value of stress in current iteration can take either the value from the last Newton-Krylov iteration or from the converged value at the end of the previous time step. Given the slow kinetics nature of ASR reactions, these two options provide essentially the same results as long as the time step size remains reasonably small, e.g., on the order of a few days. However, for large time steps, the stress value from the last Newton-Krylov iteration should be used for calculating $\Delta\epsilon^{ASR}$. Grizzly by default uses the converged stresses at the end of the previous time step, and users can optionally override this option to use the value from the previous iteration.

To summarize, during each time step, within each globe Newton-Krylov iteration, on each quadrature point within each element, an incremental ASR reaction extent $\Delta\xi$ is calculated first by numerically solving Equation 76 via a local Newton iteration procedure; then an incremental ASR volumetric strain $\Delta\epsilon_{vol}^{ASR}$ is computed next using Equation 77, followed by the calculations of expansion redistribution weights using Equation 82 and ASR incremental strains $\Delta\epsilon_i^{ASR}$ using Equation 87 for principal directions; and finally the full ASR-induced incremental strain tensor $\Delta\epsilon^{ASR}$ is obtained using Equation 88.

4.6 Validation of the ASR swelling model

Multon and Toutlemonde [81] presented experimental measurements of concrete specimens subjected to ASR swelling under various confinement and stress states to better quantify the effects of stress on ASR expansion anisotropy. These experimental measurements are used to validate the anisotropic ASR swelling model implemented in Grizzly. In Multon and Toutlemonde's experiments, cylindrical concrete specimens of 130mm in diameter and 240mm in height are confined by stacks of steel rings, as shown in Figure 14. In their experiments, two types of steel rings, 3mm and 5mm in thickness, were used. The data obtained from the tests using 3mm-thick steel ring confinements were chosen to compare against the simulations. Also it is worth noting that because stacks of steel rings are used to provide lateral confinements, the steel rings do not provide any constraint to the movement of specimens along the axial direction. A frictionless contact model between the specimens and steel rings is adopted in the simulations to represent that condition. Three levels

31

of the applied axial loading stresses, 0, 10 and 20 MPa, are chosen from the experiments to compare against simulations.
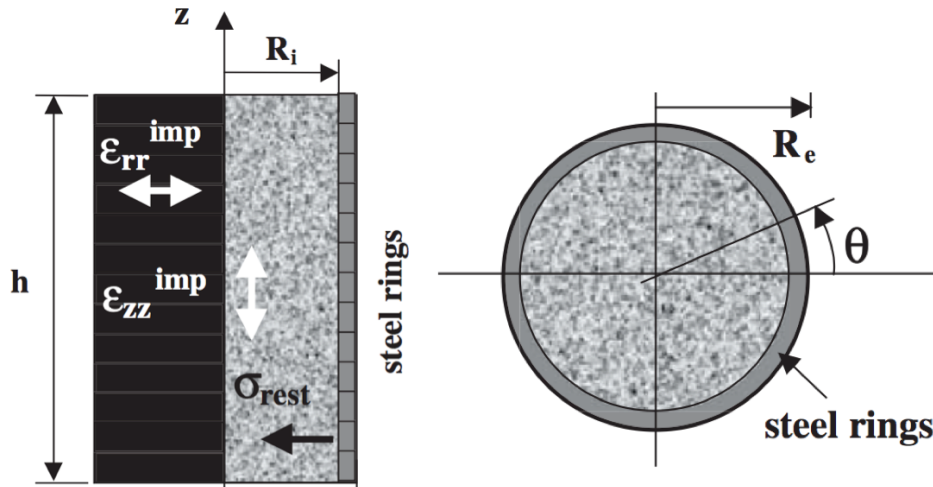

Figure 14: Schematic description of Multon and Toutlemonde's ASR expansion experiments [81]: (left) axial view and (right) plane view.

All tests were carried out under isothermal conditions (room temperature) and constant and uniform relative humidity H of 1 for all specimens. All mechanical deformations of specimens are induced by the axial stress (if any exist) and ASR reactions. Table 7 lists the parameters used in this ASR model validation study.

4.6.1   ASR expansion without steel ring confinement

The first ASR expansion experiments to be simulated were those conducted by Multon and Toutlemonde [81] in which no lateral confinement was applied, and various axial stresses (0, 10 and 20 MPa) were applied to the specimens. Due to the axially symmetry of the sample geometry and loading conditions, the problem was simulated by using a 2D axisymmetric model with half of the height of the specimens, a roller boundary on the bottom (zero displacement in the axial direction) and a roller boundary on the left (zero displacement in radial direction), and free movement (i.e. stress free) boundary condition on the right edge. Figure 15 shows the boundary conditions of the 2D axisymmetric model and the finite element mesh used in the simulations.

Since there is no lateral confinement, in all 3 different loading scenarios (uniaxial stress states), the stress, ASR reaction extent and associated ASR induced strain are uniform within the specimen at any given moment. However, the magnitudes of ASR reaction extent and ASR strain could be different under different loading conditions. Figure 16 shows comparisons of the ASR reaction extent and ASR-induced volumetric strain with three different loading stresses. It is quite obvious that the increase in the axial loads retarded the ASR reaction and resulted in smaller ASR volumetric strain (i.e., less volumetric expansion induced by ASR). This result is consistent with experimental observations.

Figure 17 shows comparisons of ASR strains in the axial and lateral directions for all three loading stresses. First, as the axial loading stress increased from 0 to 10 MPa, despite the small reduction of total ASR volumetric strain, the lateral ASR strain increases (Figure 17-left). This can be explained by the fact that when the axial loading stress increased, the compressive stress along the axial direction suppressed the axial ASR strain (Figure 17-right), and redistributed the ASR volumetric strain to the lateral direction along
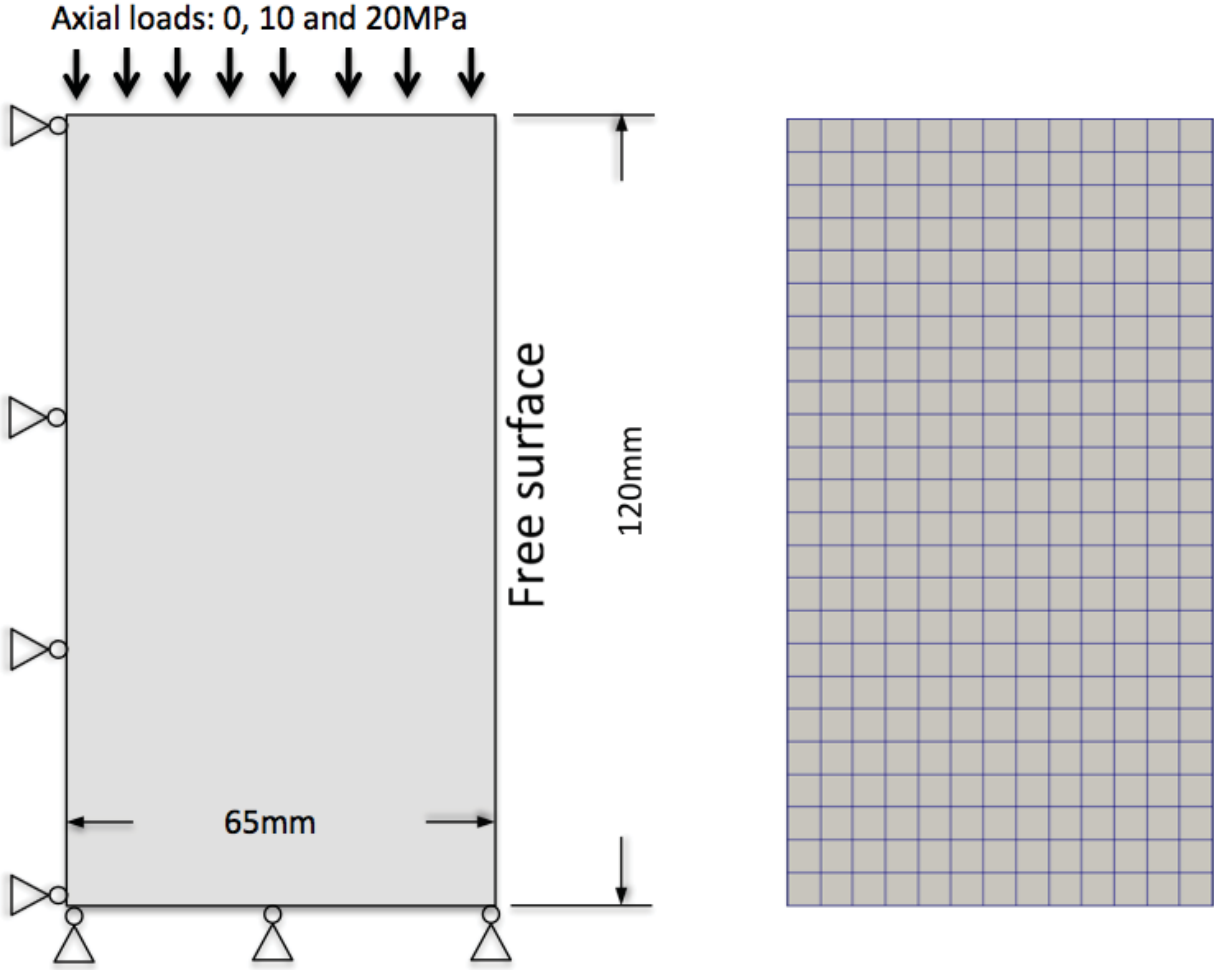
Figure 15: Schematic descriptions of geometry and boundary conditions of the 2D axial symmetric model (left) and the finite element mesh used in the simulations.
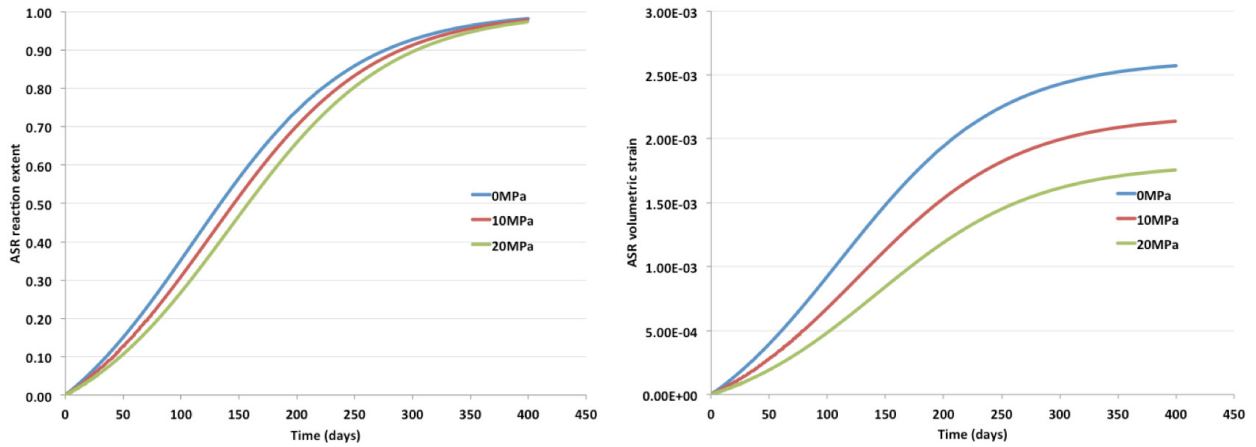

Figure 16: Temporal evolution of the ASR reaction extent (left) and ASR volumetric strain (right) for three axial loading stresses, 0, 10 and 20 MPa.

Table 7: General parameters of the ASR model (following [81] and [35])

Characteristics	Symbol	Unit	Value
Maximum volumetric ASR strain at test temperature T_0^{test}	ε^∞	–	0.00262
Characteristic time at test temperature T_0^{test}	τ_C	day	68.9
Latency time at test temperature T_0^{test}	τ_L	day	110.0
Activation energy associated with τ_C	U_C	K	5,400
Activation energy associated with τ_L	U_L	K	9,400
Residual reduction factor	Γ_r	–	0.5
Tensile strength	f'_t	MPa	3.2
Residual reduction factor for ASR expansion under tensile stress	γ_r	–	0.5
Fraction of f'_t prior to reduction of ASR expansion due to macro-cracking	γ_t	–	0.5
Compressive strength	f'_c	MPa	−31
Factor of retardation of ASR reaction under compression in Eq. 75	α	–	4/3
Shape parameter of ASR expansion reduction under compression in Eq. 80	β	–	0
Upper compressive stress beyond which there is no more ASR expansion	σ_u	MPa	−8
Concrete Young's modulus	E_0	GPa	37.3
Concrete Poisson's ratio	ν	–	0.22
Reduction fraction for Young's Modulus at end of ASR reaction	β_E	–	0.5
Reduction fraction for tensile strength at end of ASR reaction	β_f	–	0.5

which the stress is zero since there is no lateral confinement. Therefore, higher ASR strain is observed in the lateral direction at 10 MPa axial load (Figure 17-left). However, when the axial load increased further to 20 MPa, the lateral ASR strain decreases from that of 10 MPa axial load case. This is due to the further reduction of the total ASR volumetric strain when the axial load increased from 10 to 20 MPa (as shown in Figure 16). It is worth noting that with no axial stress, both the axial and lateral ASR strains are the same, exhibiting an isotropic swelling behavior. This is consistent with the stress free state.
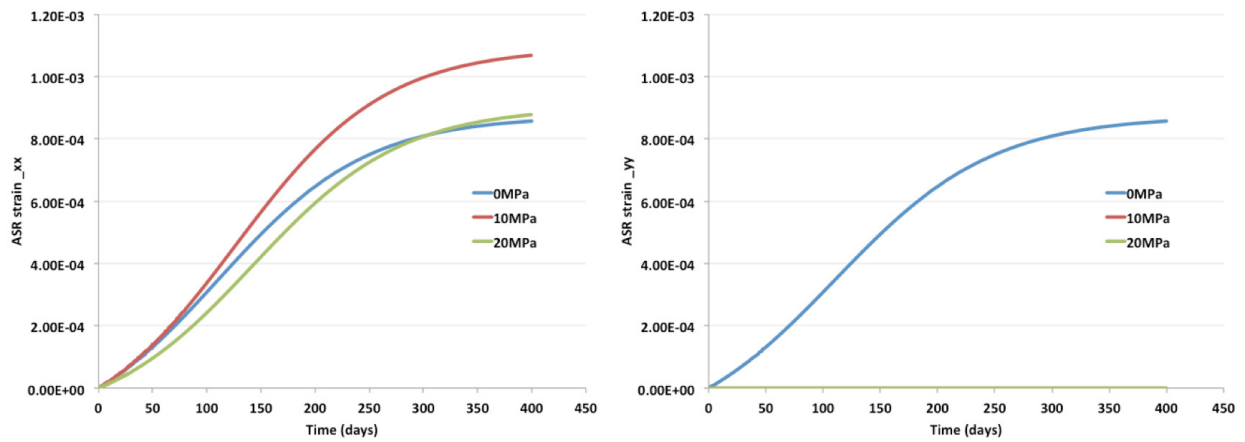

Figure 17: Comparisons of the ASR strains in lateral (left) and axial (right) directions for three axial loading stresses, 0, 10 and 20 MPa.

Figure 18 shows the comparisons of the axial and lateral displacements for all three loading stresses.

These results are consistent with the previous ASR strain results shown in Figure 17.
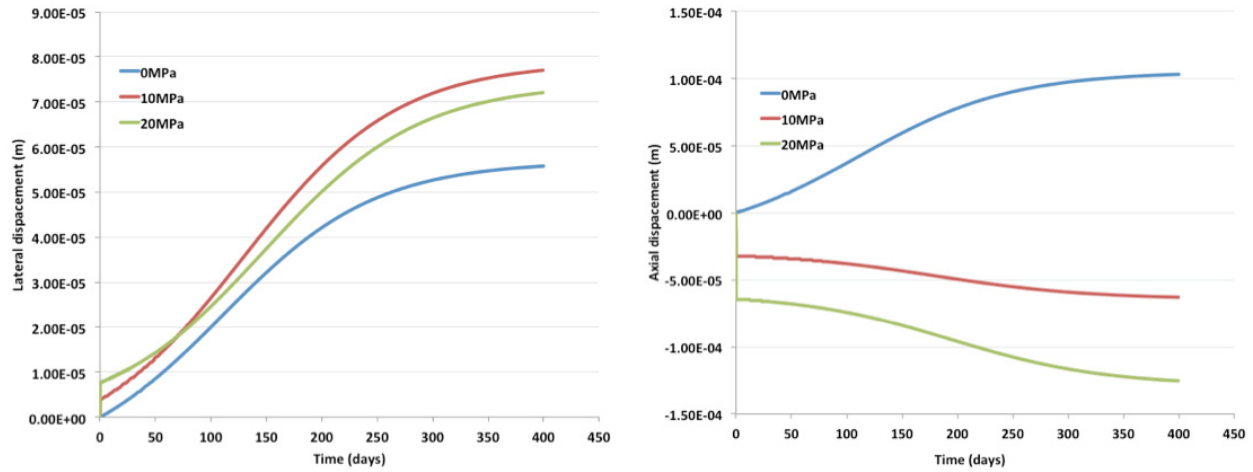

Figure 18: Comparisons of the displacements in lateral (left) and axial (right) directions for three axial loads, 0, 10 and 20 MPa.

In this model validation study, three ASR expansion parameters, characteristic time τ_C, latency time τ_L and maximum ASR volumetric strain ε^∞ under free expansion condition, are calibrated using the lateral strains measured on the specimens under no axial stress, similar to [35]. The values of these three parameters listed in Table 7 are the values after calibration. Figure 19 shows the comparisons between the simulated (lines) and measured (symbols) lateral strains from [81] for all three loading stresses. It is not surprising that the simulated lateral strain under no axial stress agrees very well with the measurements since the ASR model parameters were calibrated against the data measured from specimens under no axial stress. The simulated lateral strain under 20 MPa axial load agrees reasonably well with the measurements by using the same set of calibrated ASR model parameters. However, the match between the measured and simulated lateral strains for 10 MPa axial load case is not satisfactory at all by using the same set of calibrated ASR model parameters. More efforts will be needed to better calibrate the ASR related model parameters against the experimental data. It should be noted that more comprehensive examinations of Multon and Toutlemonde's experimental data [81] and the ways how their data were processed and presented will be necessary for further model validation effort. For example, these simulations clearly show the instantaneous lateral strains at 10 and 20MPa loads, however, the experimental data does not show such instantaneous lateral strain due to axial loads.

4.6.2   ASR expansion with steel ring confinement

The Grizzly ASR model was also used to simulate Multon and Toutlemonde's ASR expansion tests with 3*mm*-thick steel ring confinement [81]. Figure 20 shows the geometry and boundary conditions of the 2D axial symmetric model and the finite element mesh used in the simulation. The steel ring is assigned a Young's modulus of 193 GPa, Poisson's ratio of 0.3, and yield stress stress of 206 MPa. Since the steel rings were not connected during the experiments, the steel rings do not constrain the axial movement of the specimens. To more realistically represent this experimental setup, a frictionless contact model (previously implemented in Grizzly) is used for better representation of the constraint provided by these unconnected steel rings.

The case of 10 MPa axial stress is used as an example to illustrate the displacement, ASR strain, stress
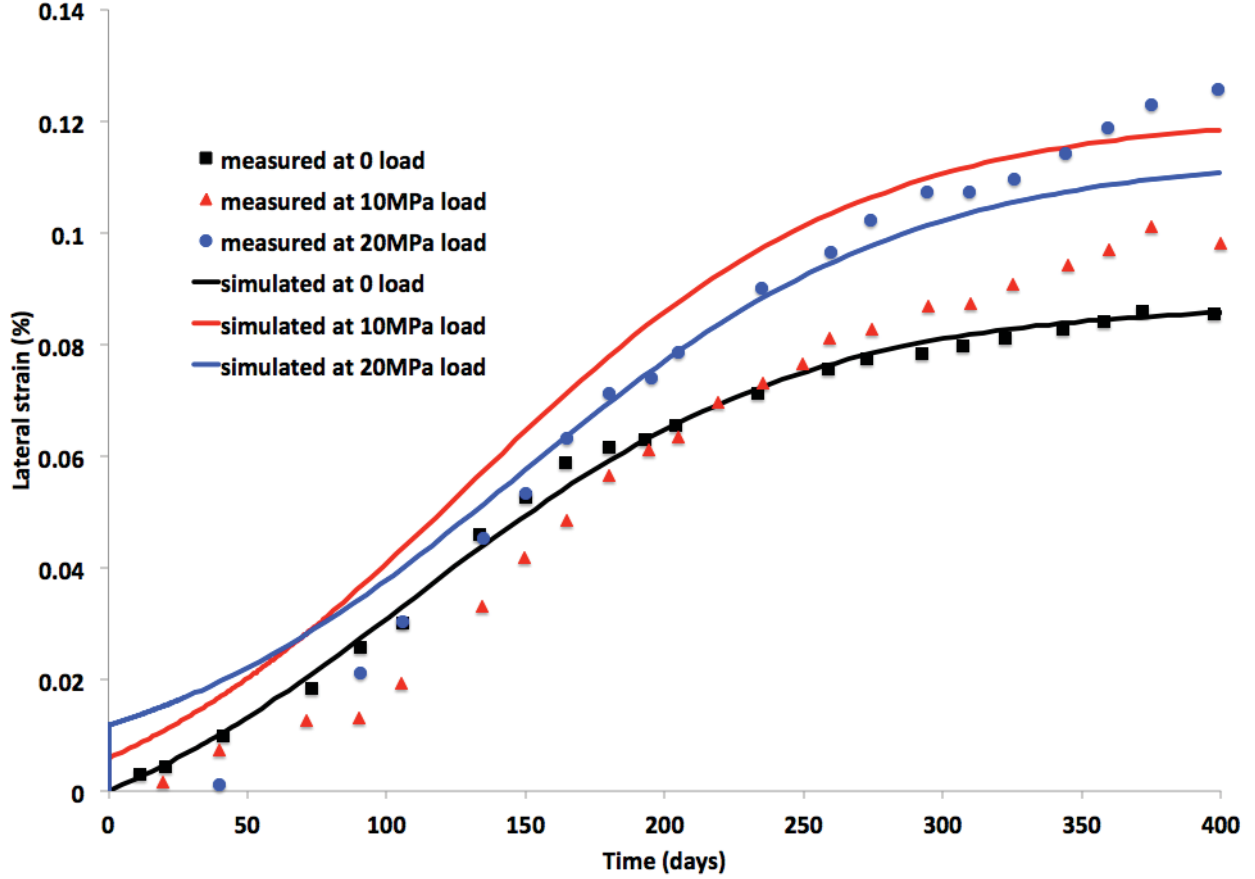
Figure 19: Comparisons of the measured and simulated lateral strains of specimens without confinement under three axial loads, 0, 10 and 20 MPa.

fields. The specimen was under true triaxial stress state when axial load was applied during the experiment. Two important parameters: α in Equation 75 and β in Equation 80, representing the retardation of reaction kinetics and the reduction of ASR-induced expansion when the specimens are under compressive stress state, need to be adjusted to match the experimental data. The measured lateral strains of the specimens subjected to 10 MPa axial load were used to calibrate α in Equation 75 and β in Equation 80, while the rest of the ASR model parameters are kept the same as those listed in Table 7. The final optimal values for α and β are 4.3 and 1.5, respectively, which yields the best match with the experimental data.

Figure 21 shows the simulated axial and lateral stress fields at a time of 400 days. The simulated axial stress in the specimen is 10 MPa, as expected, to be equal to the applied load, and uniform everywhere. the lateral (or radial) stress in the specimen is about -4.7 MPa, smaller that the axial stress and uniform everywhere within the specimen. The axial stress in the steel rings is 0, which is consistent with the frictionless contact model used for the concrete-steel interface.

Figure 22 shows the simulated axial and lateral displacement fields at a time of 400 days. Note the discontinuity of the axial displacement field across the concrete-steel ring interface due to the frictionless contact model used in the simulations. The simulated lateral displacement, however, is continuous across the concrete-steel interface.

Figure 23 shows the simulated axial and lateral ASR strains (e.g., the chemical strains imposed onto the concrete structures) at a time of 400 days. Note that the axial ASR strain is about an order of magnitude
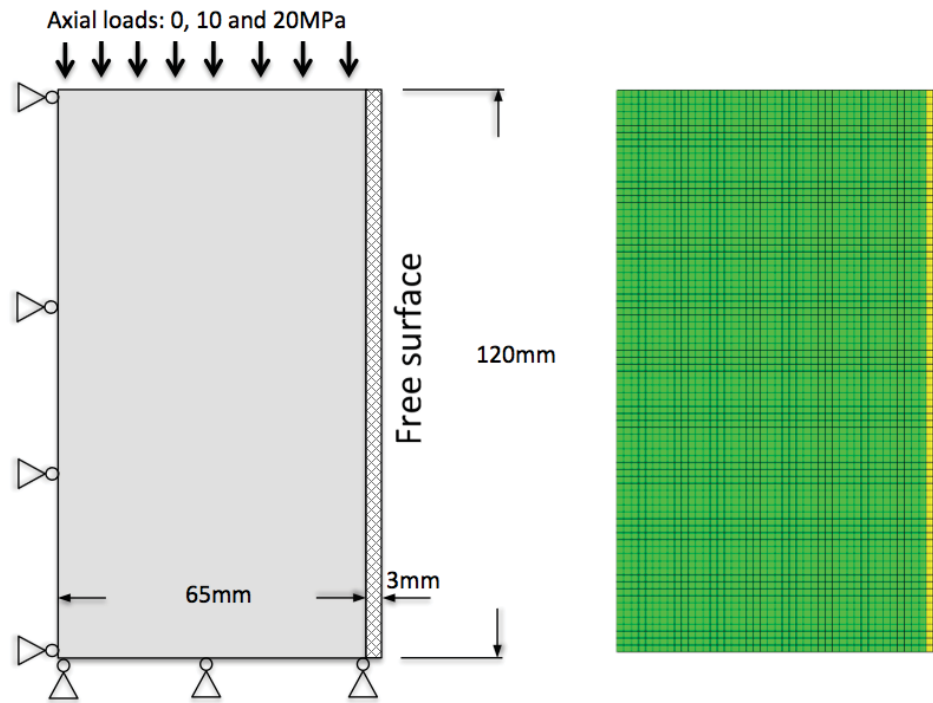
Figure 20: Geometric and boundary conditions (left) and finite element mesh (right) for simulating the ASR expansion experiments with steel ring confinement.
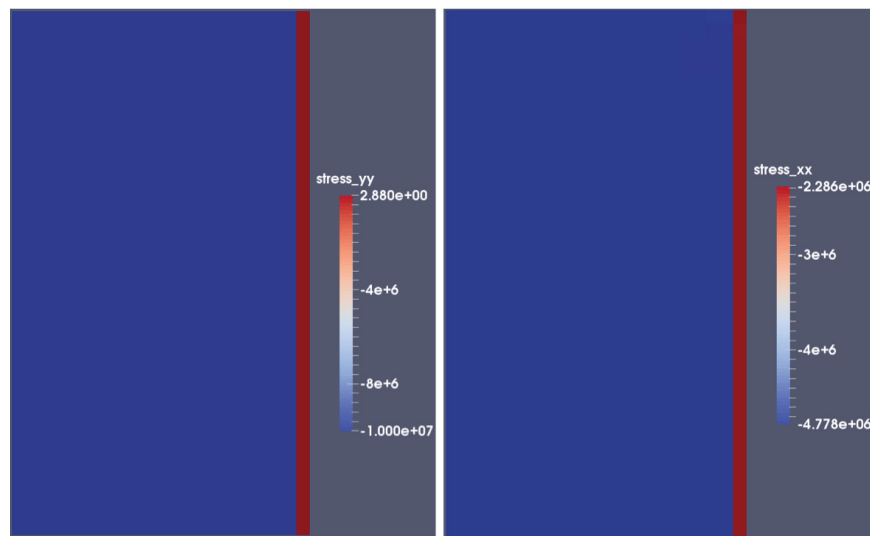

Figure 21: The axial (left) and lateral (right) stresses at time of 400 days.
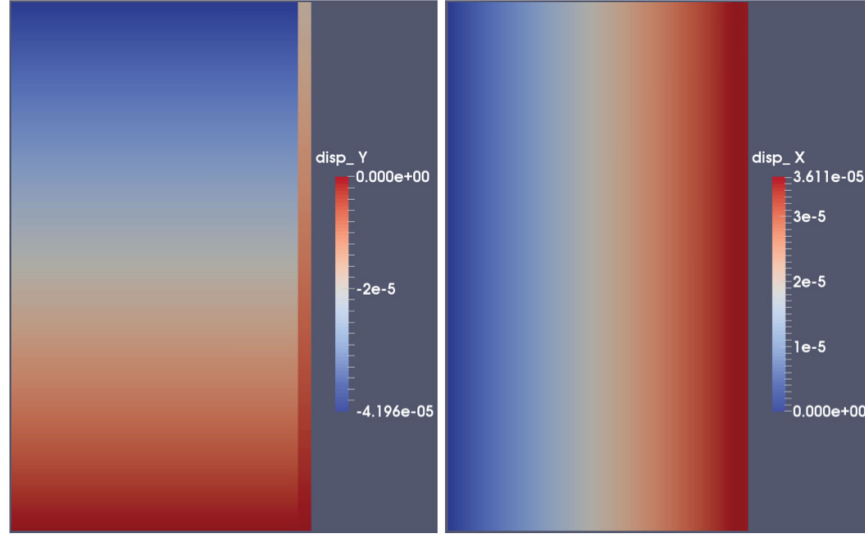
Figure 22: The axial (left) and lateral (right) displacements at time of 400 days.

smaller than the lateral ASR strain due to much higher stress in the axial direction than the lateral direction.
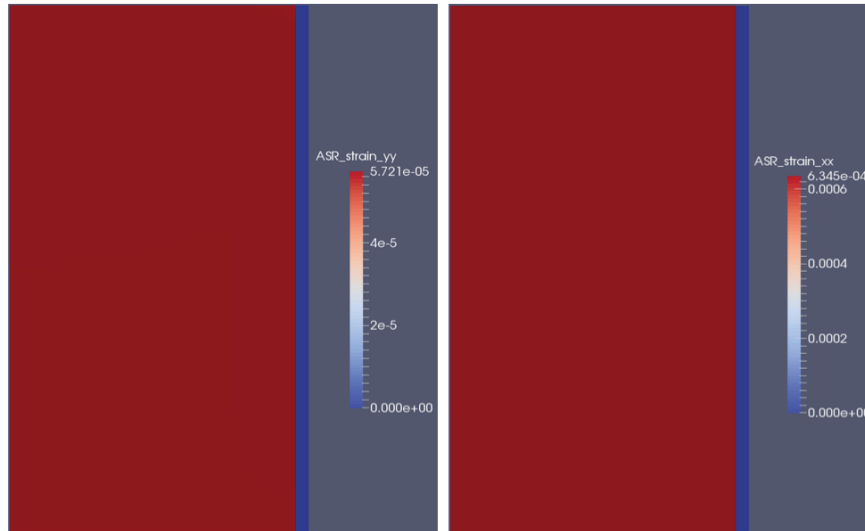
Figure 23: The axial (left) and lateral (right) ASR strains at time of 400 days.

Figure 24 shows a detailed comparison of simulated and measured lateral strains for the specimens confined by 3 mm thick steel rings and subjected to 10 and 20 MPa axial loading stresses. For the case of 10 MPa axial stress, the simulated lateral strain agrees with the experimental very well. This is not surprising since the model was calibrated to the data measured at 10 MPa axial stress. When using the same parameter values of α and β to simulate the experiments with 20 MPa axial stress, a reasonably satisfactory match to the experimental data is obtained.

Saouma and Perotti [35] performed similar comparison study using the same experimental data from [81], and obtained an optimal value of 0.5 for β. However, Saouma and Perotti [35] did not provide the full list of their model parameters used in their simulations. It is also unclear how they modeled the effects
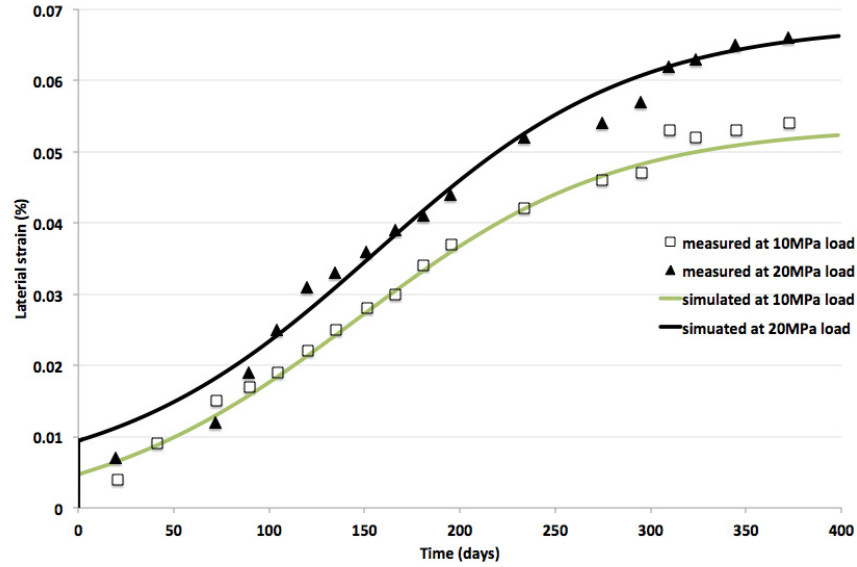
Figure 24: Comparisons between the simulated and measured lateral strains for confined specimens at 10 and 20 MPa axial loading stresses

of confining steel rings. Therefore it is not surprising that our model calibration exercise yields different calibrated parameter values. Again, it is also not clear from [81] how the raw measurement data for specimens with steel ring confinement were "processed" and presented. It is necessary to more carefully examine the measured data reported in [81], or choose other better documented test data for future model validation efforts.

5 Summary and Recommendations

When long term operation is considered for nuclear power plants, it is critical to have accurate and reliable predictive tools to address concerns related to various aging processes of concrete structures and the capacity of the structures subjected to aging-related degradation. For this reason, development was initiated on a fully coupled thermo-hydro-mechanical-chemical (THMC) concrete model in Grizzly, with the ultimate goal of reliably modeling and predict long-term performance and response of concrete structures in nuclear power plants subjected to various aging and degradation mechanisms.

Three concrete modules have been implemented in Grizzly to address concerns of aging and degradation of concrete structures due to various internal and (or) external chemical attacks: (1) a multi-species reactive diffusion model within cement materials; (2) a coupled moisture and heat transfer model for concrete; and (3) an anisotropic, stress-dependent, alkali-silica reaction induced swelling model. The multi-species reactive diffusion model was implemented with the objective of modeling aging of concrete structures subjected to aggressive external chemical attacks (e.g., chloride attack, sulfate attack etc.). The moisture/heat transfer module was implemented to simulate long-term spatial and temporal evolution of the moisture and temperature fields within concrete structures at both room and elevated temperatures. The ASR swelling model implemented in Grizzly simulates anisotropic expansions of ASR gel under either uniaxial, biaxial and triaxial stress states, and can be run simultaneously with the moisture/heat transfer model and coupled with various elastic/inelastic solid mechanics models that were implemented in Grizzly previously. The simulation results of various example problems and preliminary model validation studies clearly demonstrate the potential of these concrete models in Grizzly for reliable evaluation and prediction of long-term aging processes and the response of aged concrete structures in nuclear power plants.

The code development effort has to this point been mainly focused on developing basic simulation capabilities for the diffusion of moisture and heat within concrete structures, penetration of chemicals from external environment (e.g., soils and groundwater) and ASR-induced anisotropic swelling. However, development has not begun on simulation capabilities for modeling the mechanical response of degraded concrete structures. More specifically, there is no capability to model the evolution of damage (in the forms of both micro- and macro-cracks) within concrete structures induced by various physical and chemical aging processes. In addition, there are no constitutive models describing how the evolution of damage within concrete structures modifies the transport properties for moisture, heat and chemicals, which in turn could possibly accelerate degradation processes. Thus, based on the initial work documented in this report and a number of survey reports of concrete aging mechanisms relevant to nuclear power plants and recommendations from researchers in the related fields, the following additional code developments and modeling studies are recommended in the near future:

- **Nonlinear mechanical constitutive models for concrete**
  The solid mechanics models in MOOSE currently have a capability to represent smeared cracking in conjunction with other models such as plasticity, but this has not yet been applied in the context of concrete modeling. A logical path forward for concrete model development is to develop a plasticity-based model for nonlinear behavior of concrete in the compressive regime that can be combined with this smeared cracking model. This should then also be combined with damage mechanics concepts to correctly capture stiffness degradation.

  Once the continuum models are implemented, development work currently underway to represent fractures as discrete discontinuities using the extended finite element method (XFEM) in MOOSE for other applications should be leveraged to improve the representation of fracture localization. Continuum models would represent concrete in the compressive regime and the initial process of fracture localization, and then XFEM would be used to represent mesh-independent localization.

- **Including effects of degradation on mechanical constitutive response**
  Once models are developed for the nonlinear mechanical constitutive response of concrete, these need to be extended to incorporate the effects of aging mechanisms on the mechanical properties of concrete.

- **Models for reinforcing steel and interaction with concrete**
  Another important area where development is needed is for modeling reinforcing steel and its interaction with concrete. Representing steel either as a smeared continuum or discrete bars is fairly straightforward, and both techniques will be useful for various structural configurations.

- **Models for radiation-induced volumetric expansion**
  Given the high priority of improving the understanding of irradiation-induced degradation mechanisms, implementing models for radiation-induced volumetric expansion and coupling those with appropriate mechanical constitutive models is recommended.

- **Nonlinear coupling between concrete cracking and transport of moisture and chemicals**
  Micro- and macro-cracks within concrete structures induced by various volume-changing degradation mechanisms can significantly promote the transport of moisture and aggressive chemicals from external environments, which in turn can further accelerate the rates of chemical reactions and degradation processes. Such coupling between cracking and reactions is critical for reliable predictions of the long-term degradation processes and durability of degraded structures. Therefore, it is recommended that models for coupling between mechanical damage and transport be developed.

- **Model validation**
  The results presented here represent an initial effort to validate transport and ASR expansion models in conjunction with their development. Much more extensive validation efforts are needed to ensure that these models and the parameters used with them provide reliable simulations of real-world concrete degradation scenarios, especially as more sophisticated models with more coupling between physics are developed.

6 References

1. D. J. Naus. Concrete component aging and its significance relative to life extension of nuclear power plants. NUREG/CR-4652, ORNL/TM-10059, Oak Ridge National Laboratory, Oak Ridge, TN 37381, 1986.

2. Mark J. Do and Alan D. Chockie. Aging degradation of concrete structures in nuclear power plants. SKI Report 94:15, Battelle Seattle Research Center, Seattle, WA 98105, 1994.

3. D. J. Naus, C. B. Oland, and B. R. Ellingwood. Report on aging of nuclear power plant reinforced concrete structures. NUREG/CR-6424, BNL-NUREG-13148, Oak Ridge National Laboratory, Oak Ridge, TN 37381, 1996.

4. D. L. Fillmore. Literature review of the effects of radiation and temperature on the aging of concrete. INEEL/EXT-04-02319, Idaho National Engineering and Environmental Laboratory, 2004.

5. Benjamin Spencer and Hai Huang. Survey of models for concrete degradation. INL/EXT-14-32925, Idaho National Laboratory, Idaho Falls, ID, August 2014.

6. JE Gillott. Alkali-aggregate reactions in concrete. *Engineering Geology*, 9(4):303–326, 1975.

7. Benoit Fournier and Marc-André Bérubé. Alkali-aggregate reaction in concrete: a review of basic concepts and engineering implications. *Canadian Journal of Civil Engineering*, 27(2):167–191, 2000.

8. TV Blosser, GW Bond, LA Lee, DT Morgan, JF Nichols, RC Reid, AB Reynolds, TOP Speidel, DW Vroom, and MA Welt. A study of the nuclear and physical properties of the ornl graphite reactor shield. , Oak Ridge National Lab., Tenn., 1958.

9. HK Hilsdorf, J Kropp, and HJ Koch. The effects of nuclear radiation on the mechanical properties of concrete. *ACI Special Publication*, 55, 1978.

10. LB Miller, RE Jarka, and DC Kaul. Study of radiation dosage to structural components in nuclear reactors. *Final Report Science Applications, Inc., Rolling Meadows, IL.*, 1, 1976.

11. Shamsad Ahmad. Reinforcement corrosion in concrete structures, its monitoring and service life prediction—-a review. *Cement and Concrete Composites*, 25(4):459–471, 2003.

12. Adam Neville. Chloride attack of reinforced concrete: an overview. *Materials and Structures*, 28(2):63–70, 1995.

13. Vinod Kumar. Protection of steel reinforcement for concrete-a review. *Corrosion Reviews*, 16(4):317–358, 1998.

14. Arnon Bentur, Neal Berke, and Sidney Diamond. *Steel corrosion in concrete: fundamentals and civil engineering practice*. CRC Press, 1997.

15. Byung Hwan Oh, Soo Won Cha, Bong Seok Jang, and Seung Yup Jang. Development of high-performance concrete having high resistance to chloride penetration. *Nuclear Engineering and Design*, 212(1):221–231, 2002.

16. P Castro, EI Moreno, and J Genescá. Influence of marine micro-climates on carbonation of reinforced concrete buildings. *Cement and Concrete Research*, 30(10):1565–1571, 2000.

17. Adam Neville. The confused world of sulfate attack on concrete. *Cement and Concrete Research*, 34(8):1275–1296, 2004.

18. Jan Skalny and PW Brown. *Sulfate attack on concrete*. Taylor & Francis, 2002.

19. P Kumar Mehta. Mechanism of sulfate attack on portland cement concrete—another look. *Cement and Concrete Research*, 13(3):401–406, 1983.

20. Anna V Saetta, Bernhard A Schrefler, and Renato V Vitaliani. The carbonation of concrete and the mechanism of moisture, heat and carbon dioxide flow through porous materials. *Cement and Concrete Research*, 23(4):761–772, 1993.

21. DWS Ho and RK Lewis. Carbonation of concrete and its prediction. *Cement and Concrete Research*, 17(3):489–504, 1987.

22. ACI Committee 318. Building code requirements for structural concrete and commentary. ACI 318-11, American Concrete Institute, Detroit, MI, 2011.

23. J Marchand, E Samson, Y Maltais, and JJ Beaudoin. Theoretical analysis of the effect of weak sodium sulfate solutions on the durability of concrete. *Cement and Concrete Composites*, 24(3):317–329, 2002.

24. F Adenot and M Buil. Modelling of the corrosion of the cement paste by deionized water. *Cement and Concrete Research*, 22(2):489–496, 1992.

25. Y Maltais, E Samson, and J Marchand. Predicting the durability of portland cement systems in aggressive environments—laboratory validation. *Cement and Concrete Research*, 34(9):1579–1589, 2004.

26. Laurent De Windt, Delphine Pellegrini, and Jan Van Der Lee. Coupled modeling of cement/claystone interactions and radionuclide migration. *Journal of contaminant hydrology*, 68(3):165–182, 2004.

27. Micheline Moranville, Siham Kamali, and Emmanuel Guillon. Physicochemical equilibria of cement-based materials in aggressive environments—experiment and modeling. *Cement and Concrete Research*, 34(9):1569–1578, 2004.

28. David Planel. *Les effets couplés de la précipitation d'espèces secondaires sur le comportement mécanique et la dégradation chimique des bétons*. PhD thesis, Marne-la-Vallée, 2002.

29. B Bary. Simplified coupled chemo-mechanical modeling of cement pastes behavior subjected to combined leaching and external sulfate attack. *International journal for numerical and analytical methods in geomechanics*, 32(14):1791–1816, 2008.

30. Barbara Lothenbach, Benoît Bary, Patrick Le Bescop, Thomas Schmidt, and Nikos Leterrier. Sulfate ingress in portland cement. *Cement and Concrete Research*, 40(8):1211–1225, 2010.

31. Jacob Bear and Y Bachmat. A generalized theory on hydrodynamic dispersion in porous media. In *IASH Symposium on Artificial Recharge and Management of Aquifers*, volume 72, pages 7–16, 1967.

32. Jacob Bear. *Dynamics of fluids in porous media*. Courier Dover Publications, 2013.

33. Yunping Xi and Zdenek P Bazant. Modeling chloride penetration in saturated concrete. *Journal of Materials in Civil Engineering*, 11(1):58–65, 1999.

34. Thomas J Wolery. Eq3/6, a software package for geochemical modeling of aqueous systems: package overview and installation guide (version 7.0). 1992.

35. Victor Saouma and Luigi Perotti. Constitutive model for alkali-aggregate reactions. *ACI Materials Journal*, 103(3), 2006.

36. Victor E Saouma. *Numerical modelling of alkali aggregate reaction*. CRC Press Inc, Boca Raton, Fla., 2014.

37. Franz-Josef Ulm, Olivier Coussy, Li Kefei, and Catherine Larive. Thermo-chemo-mechanics of asr expansion in concrete structures. *Journal of engineering mechanics*, 126(3):233–242, 2000.

38. Anna V Saetta, Bernhard A Schrefler, and Renato V Vitaliani. 2 - d model for carbonation and moisture/heat flow in porous materials. *Cement and Concrete Research*, 25(8):1703–1712, 1995.

39. S. Dal Pont, S. Durand, and B.A. Schrefler. A multiphase thermo-hydro-mechanical model for concrete at high temperatures—finite element implementation and validation under LOCA load. *Nuclear Engineering and Design*, 237(22):2137–2150, November 2007.

40. F Bangert, D Kuhl, and G Meschke. Chemo-hygro-mechanical modelling and numerical simulation of concrete deterioration caused by alkali-silica reaction. *International Journal for Numerical and Analytical Methods in Geomechanics*, 28(7-8):689–714, 2004.

41. Detlef Kuhl, Falko Bangert, and Günther Meschke. Coupled chemo-mechanical deterioration of cementitious materials. part i: Modeling. *International Journal of Solids and Structures*, 41(1):15–40, 2004.

42. Detlef Kuhl, Falko Bangert, and Günther Meschke. Coupled chemo-mechanical deterioration of cementitious materials part ii: Numerical methods and simulations. *International Journal of Solids and Structures*, 41(1):41–67, 2004.

43. B Bary and A Sellier. Coupled moisture—carbon dioxide–calcium transfer model for carbonation of concrete. *Cement and concrete research*, 34(10):1859–1872, 2004.

44. George Chatzigeorgiou, Vincent Picandet, Abdelhafid Khelidj, and Gilles Pijaudier-Cabot. Coupling between progressive damage and permeability of concrete: analysis with a discrete model. *International journal for numerical and analytical methods in geomechanics*, 29(10):1005–1018, 2005.

45. P Kumar Mehta and Ben C Gerwick. Cracking-corrosion interaction in concrete exposed to marine environment. *P. K. Mehta and B. C. Gerwick, Jr., Concrete International: Design & Construction, V. 4,*, (10):45–51, 1982.

46. Franz-Josef Ulm, Eric Lemarchand, and Franz H Heukamp. Elements of chemomechanics of calcium leaching of cement-based materials at different scales. *Engineering Fracture Mechanics*, 70(7):871–889, 2003.

47. P Léger, P Côté, and R Tinawi. Finite element analysis of concrete swelling due to alkali-aggregate reactions in dams. *Computers & structures*, 60(4):601–611, 1996.

48. HJ Dagher and S Kulendran. Finite element modeling of corrosion damage in concrete structures. *ACI Structural Journal*, 89(6), 1992.

49. O Burkan Isgor and A Ghani Razaqpur. Finite element modeling of coupled heat transfer, moisture transport and carbonation processes in concrete structures. *Cement and Concrete Composites*, 26(1):57–73, 2004.

50. S. Dal Pont, F. Meftah, and B.A. Schrefler. Modeling concrete under severe conditions as a multiphase material. *Nuclear Engineering and Design*, 241(3):562–572, March 2011.

51. Mike B Otieno, Hans D Beushausen, and Mark G Alexander. Modelling corrosion propagation in reinforced concrete structures–a critical review. *Cement and Concrete Composites*, 33(2):240–245, 2011.

52. D Gawin, F Pesavento, and BA Schrefler. Modelling of hygro-thermal behaviour of concrete at high temperature with thermo-chemical and mechanical material degradation. *Computer methods in applied mechanics and engineering*, 192(13):1731–1771, 2003.

53. Alain Millard, Valerie L'Hostis, Karim BEDDIAR, Yves Berthaud, and Sabine Care. Modelling the cracking of a reinforced concrete structure submitted to corrosion of steels-first validation of a damage model based on experimental results. 2004.

54. Zdeněk P Bažant. Prediction of concrete creep and shrinkage: past, present and future. *Nuclear Engineering and Design*, 203(1):27–38, 2001.

55. Y Ichikawa and GL England. Prediction of moisture migration and pore pressure build-up in concrete at high temperatures. *Nuclear Engineering and Design*, 228(1):245–259, 2004.

56. Miguel Cervera, Javier Oliver, and Tomás Prato. Thermo-chemo-mechanical model for concrete. i: Hydration and aging. *Journal of engineering mechanics*, 125(9):1018–1027, 1999.

57. Miguel Cervera, Javier Oliver, and Tomás Prato. Thermo-chemo-mechanical model for concrete. ii: Damage and creep. *Journal of engineering mechanics*, 125(9):1028–1039, 1999.

58. D Gawin, F Pesavento, and BA Schrefler. Towards prediction of the thermal spalling risk through a multi-phase porous media model of concrete. *Computer methods in applied mechanics and engineering*, 195(41):5707–5729, 2006.

59. Zdeněk P Bažant and Werapol Thonguthai. Pore pressure in heated concrete walls: theoretical prediction. *Magazine of Concrete Research*, 31(107):67–76, 1979.

60. Zdeněk P Bažant, Jenn-Chuan Chern, and Werapol Thonguthai. Finite element program for moisture and heat transfer in heated concrete. *Nuclear Engineering and Design*, 68(1):61–70, 1982.

61. Yunping Xi, Zdeněk P Bažant, and Hamlin M Jennings. Moisture diffusion in cementitious materials adsorption isotherms. *Advanced Cement Based Materials*, 1(6):248–257, 1994.

62. Yunping Xi, Zdenňek P. Bažant, Larissa Molina, and Hamlin M. Jennings. Moisture diffusion in cementitious materials moisture capacity and diffusivity. *Advanced Cement Based Materials*, 1(6):258–266, November 1994.

63. Victor Saouma, Wiwat Puatatsananon, and Yann Le Pape. Alkali-silica reaction in nuclear power plants. ORNL/TM-xxxx/xx, Oak Ridge National Laboratory, 2015.

64. Kuzman Raznjevic and Rickard Podhorsky. *Tables et diagrammes termodynamiques*. Eyrolles, 1970.

65. CA Yunus and JG Afshin. Heat and mass transfer: Fundamentals and applications, 2011.

66. ASCE. Structural fire protection, asce committee on fire protection, structural division, american society of civil engineers, new york, ny, usa. , 1992.

67. VKR Kodur, TC Wang, and FP Cheng. Predicting the fire resistance behaviour of high strength concrete columns. *Cement and Concrete Composites*, 26(2):141–153, 2004.

68. Eurocode. Design of concrete structures. part 1-2: general rules - structural fire design,. , European Committee for Standardization, Brussels, Belgium., 2004.

69. Kook-Han Kim, Sang-Eun Jeon, Jin-Keun Kim, and Sungchul Yang. An experimental study on thermal conductivity of concrete. *Cement and Concrete Research*, 33(3):363–371, 2003.

70. Roland Wynne Lewis and Bernard A Schrefler. *The finite element method in the static and dynamic deformation and consolidation of porous media*. John Wiley, 1998.

71. BA Schrefler and F Pesavento. Multiphase flow in deforming porous material. *Computers and geotechnics*, 31(3):237–250, 2004.

72. Olivier Coussy. *Poromechanics*. John Wiley & Sons, 2004.

73. Ayman Ababneh, Farid Benboudjema, and Yunping Xi. Chloride penetration in nonsaturated concrete. *Journal of Materials in Civil Engineering*, 15(2):183–191, 2003.

74. R Mensi, P Acker, and A Attolou. Séchage du béton: analyse et modélisation. *Materials and structures*, 21(1):3–12, 1988.

75. TZ Harmathy and LW Allen. Thermal properties of selected masonry unit concretes. In *ACI Journal Proceedings*, volume 70. ACI, 1973.

76. Dana A Knoll and David E Keyes. Jacobian-free newton–krylov methods: a survey of approaches and applications. *Journal of Computational Physics*, 193(2):357–397, 2004.

77. Guillaume Ranc, Jérôme Sercombe, and Sylvain Rodrigues. Comportement à haute température du béton de structure: impact de la fissuration sur les transferts hydriques. *Revue française de génie civil*, 7(4):397–424, 2003.

78. Benoît Bary, Marcus VG de Morais, Stéphane Poyet, and Sabine Durand. Simulations of the thermo-hydro-mechanical behaviour of an annular reinforced concrete structure heated up to 200° c. *Engineering Structures*, 36:302–315, 2012.

79. C. Larive. Apports combin'es de l'experimentation et de la modélisation à la comprehension del' a lcali-réaction et de ses effets mécaniques,. *PhD thesis, Thése de Doctorat, Laboratoire Central des Ponts et Chaussées, Paris.*, 1998.

80. MCR Farage, JLD Alves, and EMR Fairbairn. Macroscopic model of concrete subjected to alkali–aggregate reaction. *Cement and Concrete Research*, 34(3):495–505, 2004.

81. Stéphane Multon and François Toutlemonde. Effect of applied stresses on alkali–silica reaction-induced expansions. *Cement and Concrete Research*, 36(5):912–920, 2006.